BIO-WAX PRODUCTION FROM WATER-ASSISTED KETONIZATION OF METHYL PALMITATE OVER METAL INCORPORATED TiO_2 CATALYSTS

JETSADAGORN PITTAYATORNKUL

A THESIS SUBMITTED IN PARTIAL FULFILLMENT OF THE REQUIREMENT FOR THE DEGREE OF MASTER OF SCIENCE IN APPLIED CHEMISTRY

DEPARTMENT OF CHEMISTRY SCHOOL OF SCIENCE

KING MONGKUT'S INSTITUTE OF TECHNOLOGY LADKRABANG

2024

KMITL-2024-SC-M-012-056

Thesis Title Bio-wax production from Water-assisted ketonization of methyl palmitate to palmitone over metal incorporated TiO_2 catalysts

Student Name Jetsadagorn Pittayatornkul

Student ID 64605025

Degree Department Master of Science (Applied Chemistry)

Year 2024

Thesis Advisor Prof. Dr. Tawan Sooknoi

Thesis Co-advisor Assoc. Prof. Dr. Tosapol Maluangnont

Abstract

Ketonization of methyl palmitate to palmitone, a bio-wax, was investigated over noble metal (Pt, Ru, and Pd) incorporated TiO_2 catalysts in the presence of water under an atmospheric H_2/N_2 flow. Methyl palmitate underwent hydrolysis to palmitic acid that ketonized to palmitone over Lewis Ti^{3+} sites. The water co-feeding also suppressed hydrodeoxygenation of methyl palmitate and palmitone cracking leading to high palmitone selectivity. The incorporated metals facilitated H_2 dissociation/spillover on TiO_2 which generated more Lewis Ti^{3+} sites for higher ketonization activity. At 400 °C, 0.5Pd/TiO_2 provided ~90% conversion with >85% palmitone selectivity and >25 h stability, due to its efficient H_2 dissociation/spillover to continually recover Lewis Ti^{3+} sites. Meanwhile, 0.5Pt/TiO_2 promoted excessive hydrodeoxygenation, leading to the deactivation from CO poisoning at the metallic Pt sites. The findings of this study offer a sustainable approach for the selective production of bio-wax from renewable fatty acid methyl esters.

Keywords: ketonization, hydrolysis, methyl palmitate, palmitone, noble metals

Acknowledgments

I would like to take this opportunity to acknowledge advisors Prof. Dr. Tawan Sooknoi and co-Advisor Assoc. Prof. Dr. Tosapol Maluangnont, for their continual suggestions, graceful knowledge, and useful discussions throughout this work. In addition, I would like to sincerely appreciate the chairperson and committee members, Assoc. Prof. Dr. Siriporn Jongpatiwut, and Asst. Prof. Dr. Chaval Sriwong, for their opinions and guidance.

I am grateful to the School of Science, KMITL for the financial support of the study (Grant No. RA/TA-2564-M-013). The assistance of personnel from the Nanotechnology and Materials Analytical Instrument Service Unit (NMIS) of the College of Materials Innovation and Technology, KMITL, from The Petroleum and Petrochemical College, Chulalongkorn University, and School of Energy Science and Engineering, Vidyasirimedhi Institute of Science and Technology, are appreciated.

I would like to distribute thanks to Catalytic Chemistry Research Unit members for their contribution to the ideas, facilities, and most importantly their support.

Furthermore, I would like to express my appreciation thanks to the Department of Chemistry, School of Science, King Mongkut's Institute of Technology Ladkrabang for advanced laboratory instruments, equipment, chemicals, and accommodation. Last but not least, I would like to gratefully thank the parents and families for their encouragement throughout this work.

Jetsadagorn Pittayatornkul

Table of contents

Page

List of tables

List of figures

List of schemes

Abbreviations/Symbols

°C	Degree Celsius
XRD	X-Ray Diffraction
TPR	Temperature-Programmed Reduction
TPD	NH_3-Temperature Programmed Desorption
DR-UV	Diffuse Reflectance UV-Visible Spectroscopy
BET	Brunauer-Emmett-Teller method
ICP-MS	Inductively coupled plasma mass spectrometry
TEM	Transmission electron microscopy
XPS	X-ray photoelectron spectroscopy
GC-MS	Gas chromatograph equipped with a mass spectrometer
API	The American Petroleum Institute
FAMEs	Fatty acid methyl esters
HDO	Hydrodeoxygenation
DCO	Decarbonylation and Decarboxylation
ß	Beta
α	Alpha
SMSI	Strong metal-support interaction
kV	Kilovolt
mA	Milliampere
θ	Theta
TCD	Thermal conductivity detector
O_L	Lattice oxygen
O_v	Oxygen vacancy
O_s	Sub oxide

Chapter 1

Introduction

1.1 Research motivation

Petroleum wax (C18-C36 hydrocarbons) contains mainly saturated paraffin hydrocarbons and small amounts of naphthenic hydrocarbons from dewaxing light lubricating oil stocks, which is required for candles, wax paper, polishes, cosmetics, and electrical insulators [1,2]. However, petroleum-based waxes are non-ecologically friendly and raise greater concern about their effects on global warming, as they are non-biodegradable and contain highly toxic agents [3–7]. To avoid these problems, plant-based oil including palm oil, rapeseed oil, and soybean oil can be alternatively used as a feedstock for bio-wax [8–10]. Particularly, palm oil is a promising source of bio-chemical feedstock as it is commonly abundant in Southeast Asia. The bio-wax can be produced from the esterification and hydrogenation of palm oil with alcohol [11–16]. However, volatile organic compounds (VOCs) such as benzene and toluene and greasy residue can be released during the process. Alternatively, palm oil can be readily converted to fatty acid/fatty acid methyl ester that can be ketonized to long-chain ketone, a bio-wax with eco-friendly [8,9,15]. While fatty acid is semi-solid and difficult to handle, fatty acid methyl ester can be widely produced for biodiesel and easily processed for ketonization. As methyl palmitate is mostly abundant in palm oil methyl ester, its ketonization yields palmitone (C31 ketone) that can be easily hydrodeoxygenated to C31 hydrocarbon a bio-wax [17].

The ketonization of two esters proceeds via coupling to a β-keto ester followed by decarboxylation to a ketone over oxygen vacancies, i.e. Lewis acid sites [18–20]. However, direct ester ketonization is kinetically unfavorable due to a high energy barrier for the coupling of long-chain ester [21]. Moreover, it has been reported that the direct ester ketonization provided a lower ketone selectivity compared to the fatty acid

[15,17,21,22]. Therefore, the water can be added to produce carboxylic acid from ester via hydrolysis since the ketonization of an acid offers a **β**-keto acid intermediate with a lower activation energy. However, no report on the integrated hydrolysis and the ketonization of an ester has been found recently.

Metal oxide such as MnO_2 [18,23–25], CeO_2 [18,23–28], ZrO_2 [18,23–25,29–32], and TiO_2 [18,23–25,29,33] has been investigated on the ketonization of fatty acid or methyl ester. Among the metal oxides, anatase TiO_2 is commercially available and inexpensive, and its generation of oxygen vacancy is well-known [33–35]. However, the amount of oxygen vacancy generated over pristine TiO_2 was very low due to a limited hydrogen dissociation ability. The number of oxygen vacancies can be increased by the addition of dopants such as Ru, Pt, Pd, Ir, and Rh [36–40]. However, a preferred metal shall not act as an active site for ketonization, but rather promote H_2 spillover to generate more Lewis acid sites on the metal oxide supports upon reduction. It has been reported that the dissociation of hydrogen occurred on the metallic sites and the subsequent spillover to TiO_2 leading to more reduction of surface Ti^{3+} sites and oxygen vacancy[41–45]. Moreover, the TiO_2 supported possessed less hydrophilic properties than other metal oxides that prevent the strong water adsorption on the TiO_2 surface hence favoring catalytic activity for water-assisted ketonization [18].

In this work, the ketonization of methyl palmitate to palmitone, a bio-wax, over metal-loaded anatase TiO_2 was examined in a fixed-bed reactor under atmospheric N_2 and H_2 in the presence of water. The role of surface Ti^{3+} sites was verified by XPS, DR-UV, H_2-TPR, Raman, and NH_3-TPD. The effects of catalyst surface area, type of carrier gas (H_2 and N_2) and water co-feeding on activity and catalyst stability were investigated. Various types of noble metals (Pd, Ru, and Pt) were doped and tested for selective production of palmitone with high stability. The role of incorporated metals in the recovery of the active sites and reaction pathway for ketonization was particularly underlined.

1.2 Objectives of the study

1.2.1 To understand the promoting effect of precious metals loaded TiO_2 catalysts on the ketonization of methyl palmitate.

1.2.2 To understand the effect of carrier gas and water on ketonization activity, palmitone selectivity, and catalyst stability.

1.2.3 To obtain the optimum experimental conditions and reaction pathway for the production of bio-wax from ketonization of methyl palmitate.

1.3 Scopes of the study

1.3.1 Set up of the catalytic testing system comprising of the fixed-bed gas flow reactor for the ester-to-ketone conversion using methyl palmitate as the model compound. The catalysts include commercial anatase TiO_2 with various types/amounts of metal loaded onto it

1.3.2 Characterization of catalysts, before and spent, with the following techniques:

1.3.2.1 X-ray diffraction technique (XRD).

1.3.2.2 Temperature-programmed reduction by hydrogen gas (H_2-TPR)

1.3.2.3 Temperature-programmed desorption by ammonia gas (NH_3-TPD)

1.3.2.4 Brunauer-Emmett-Teller method (BET)

1.3.2.5 Inductively coupled plasma atomic emission spectroscopy (ICP-OES)

1.3.2.6 Transmission electron microscope (TEM)

1.3.2.7 Raman spectroscopy

1.3.2.8 X-ray photoelectron spectroscopy (XPS)

1.3.2.9 Diffused reflectance ultraviolet-visible spectroscopy (DR-UV)

1.3.2.10 Thermal gravimetric analysis (TGA)

1.3.3 Testing catalytic activity

1.3.3.1 Effect of H_2 and N_2 as a carrier gas

1.3.3.2 Effect of water vapor (partial pressure 0 and 0.24 atm)

1.3.3.3 Effect of TiO_2 supports i.e. commercial and sol-gel anatase TiO_2

1.3.3.4 Effect of Pt, Ru, and Pd loaded (0.5 wt%) on TiO_2 catalyst

1.3.3.5 Effect of contact time (58-581gh/mol)

1.3.4 Analysis of the liquid products by a gas chromatograph (GC) equipped with a mass spectrometer (GC-MS) or with a flame ionization detector and gas products analyzed by an online gas chromatograph (GC) with a thermal conductivity detector.

1.4 Benefits of the study

This work could provide the highly efficient metals promoted TiO_2-based catalysts and reaction conditions for water-assisted ketonization of saturated fatty acid methyl ester to long-chain ketone and/or bio-wax.

Chapter 2

Theory and literature reviews

2.1 Mineral wax

Mineral waxes are primarily derived from the fractional distillation of petroleum, shale oil, lignite, or coal. Common examples include paraffin, ceresin, microcrystalline wax, and petrolatum. These waxes are typically white and translucent, characterized by their stability and unreactive nature.

2.1.1 Petroleum wax

Petroleum wax is a complex mixture of long-chain hydrocarbons that contain straight, branched, and cyclic (>C20, melting point above 37 °C and boiling point above 370 °C). Paraffin wax refers to a wide range of products with hundreds of chemicals and additives including lubrication, electrical insulation, and candles dyed paraffin wax can be made into crayons. Moreover, paraffin wax is an excellent material for storing heat called phase change material (PCMs) is a substance that releases/absorbs sufficient energy at phase transition to provide useful heat or cooling [2,46–48]. There are two types of petroleum wax:

1. Paraffin wax is a white, soft, odorless solid. When mixed with solvents, it becomes sticky and soft [49].
2. Microcrystalline wax is a small crystal that is sticky and soft. It has a high molecular weight. It has a higher tensile strength and melting point than paraffin wax. It has a less shiny and slippery texture [50].

2.1.2 Montan wax

Montan wax is an extractable component of brown coal, specifically derived from coals with a bitumen content of 10-20%. The extraction process involves thermal separation, where brown coal is crushed, screened, agglomerated, and dried. Toluene is commonly used as the extracting agent, though other organic solvents can also be employed. The extraction occurs at varying temperatures and in different extractors, and the solvent is recycled post-extraction. The resulting, nearly solvent-free brown coal can be repurposed as solid fuel [51,52].

2.2 Bio wax

Bio-waxes are long-chain nonpolar lipids, primarily consisting of esters formed from fatty acids and long-chain alcohols. They are synthesized by various animals and plants.

2.2.1 Animal wax

Animal wax esters typically originate from different carboxylic acids and fatty alcohols. The specific composition of a wax can vary based on both the species of the organism and its geographic location. For example, beeswax is produced by worker bees from their wax glands and is used to construct and seal honeycombs. It appears as small, pure white flakes that are light in weight and can be clear, translucent, or colorless. Beeswax dissolves well in oils, such as turpentine, but is insoluble in water. It has a melting point of approximately 63-65 °C; heating it beyond this can pose a fire hazard. At low temperatures, beeswax shrinks and becomes brittle. Pure beeswax is commonly used in the cosmetic industry, candle making, batik processes, and as a waterproofing, polishing, and lubricating agent [53–55].

2.2.2 Plant wax

Plant waxes are waterproofing components found in an amorphous layer on the outer surfaces of plants, serving as a barrier to protect against environmental stress. They play a crucial role in plant health and have various food applications. Common types of plant waxes include candelilla wax, carnauba wax, rice bran wax, sunflower wax, soy wax, and palm wax. For example, palm wax is derived from 100% palm oil through a hydrogenation process that converts the oil into a solid wax. Candles made from palm wax feature a unique crystal pattern and are harder than soy wax candles. This makes them well-suited for creating molded or intricately shaped candles [56,57]. Normally, Plant wax compounds are complex mixtures of lipids primarily composed of aliphatic compounds with long carbon chains, typically ranging from about C20 to C60. These compounds contribute to the wax's waterproofing properties and protective functions in plants [50,58].

2.2.3 Synthesis of bio-wax

Enzymatic synthesis of wax esters can be achieved through transesterification or esterification reactions using various raw materials and commercial enzymes. Free fatty acids (FFA) obtained from the refining of vegetable oils are a promising source for this synthesis. The refining process generates by-products like soap stocks from soybean oil and palm fatty acid distillate (PFAD) from palm oil, both of which are rich in FFAs (over 85%). PFAD contains palmitic acid and other triglycerides, along with unsaponifiable components like sterols and vitamin E. Similarly, soap stock from soybean oil is high in FFAs such as linoleic, oleic, and palmitic acids, and acidulating it yields soybean fatty acid distillate (SFAD). Both PFAD and SFAD are used in various applications, including soap, oleochemicals, and animal feed, but they also have the potential to produce valuable chemicals, including lubricants and wax esters, in addition to biofuels [7,15,16].

Wax esters, part of a broader class of lipophilic organic compounds that includes hydrocarbons, ketones, and fatty aldehydes, exhibit excellent wetting properties and a non-greasy feel when applied to the skin. They are important ingredients in cosmetics (like cleansers, conditioners, and moisturizers), pharmaceuticals (acting as anti-foaming agents in penicillin production), lubricants, plasticizers, and various other chemical applications. Additionally, wax esters can be produced through the alcoholysis of vegetable oils like palm oil, which comprises triacyl glycerides made of glycerol and different fatty acids. Enzymatic synthesis methods have also been explored, such as the use of rapeseed fatty acid methyl ester and lipase-catalyzed alcoholysis of crambo and camelina oils. This versatility makes wax esters valuable components in numerous applications across various industries [59,60].

2.2 Fatty Acid Methyl Esters

Fatty acid methyl esters (FAMEs) are derived from the transesterification of fats with methanol, the most common of which are listed in **Table 2.2**. The hydrocarbon chain of FAMEs might be entirely saturated or include some double bonds. These esters have physical properties similar to petroleum-based diesel fuels rather than pure vegetable oils. This fact is reflected by its commercial use as a biodiesel, which is a renewable alternative fuel made up of a blend of several FAMEs (and certain additives). The physical characteristics of FAMEs are comparable to those of ordinary diesel. It is non-toxic and biodegradable as well [8,9,61,62]. Different FAMEs have distinguishable physical features due to differences in the amount of carbon atoms as also summarized in **Table 2.2**.

Table 2.1 Some examples of fatty acid methyl ester and their physical properties.

Chain length	Systematic Name	Trivial name	Methyl ester	
			m.p./°C	b.p./°C
11	Methyl decanoate	Methyl caprate	-14.00	108
12	Methyl undecanoate	Methyl undecylate	-	-
13	Methyl dodecanoate	Methyl laurate	-	-
14	Methyl tridecanoate	-	5.5	131
15	Methyl tetradecanoate	-	18	-
16	Methyl pentadecanoate	-	18.50	155
17	Methyl hexadecanoate	Methyl palmitate	32-35	185
18	Methyl heptadecanoate	-	-	-
19	Methyl octadecanoate	Methyl stearate	-	182
20	Methyl nonadecanoate	-	-	-

Methyl palmitate (**Fig 2.1**) will be used as a model compound in this work because it occurs naturally in crude palm oil. It is generally synthesized by the simple transesterification of triglyceride oil and methyl alcohol [23,63]. It is predicted that methyl palmitate will undergo ketonization to palmitone, a long-chain ketone that is useful in a variety of applications (**Table 2.3**). The long-chain ketone is also a precursor for the subsequent synthesis of bio-waxes and other chemicals.

Fig 2.1 Molecular structure of methyl palmitate

Table 2.2 The use of long-chain ketone in industrial applications.

Long-chain ketone in range C_{12}-C_{17}	⇒ Food additive ⇒ Fragrances or odor agents ⇒ Used to prevent cholera infection
Long-chain ketone C_{23}	⇒ Anticancer properties(breast cancer)
Long-chain ketone C_{25}	⇒ Food packaging, plates, cutlery
Long-chain ketone C_{31}	⇒ Pharmaceutical industry: Anticonvulsant Fragrances or odor agents ⇒ Toys, child use

2.3 Reactions of fatty acid methyl esters (FAMEs)

2.3.1 Thermal cracking

The simplest cracking mechanism, often occurring with double bonds of FAMEs, is thermal cracking, which is defined as the thermal degradation of organic chains by heat in an oxygen-free environment. It uses heat to break down the molecule size. The bigger hydrocarbon molecules become unstable and spontaneously break down into smaller molecules of all sizes and sorts. When the temperature is high enough, no further complexity, such as a catalyst or hydrogen, is required. The desired degree of cracking (conversion) may be somewhat controlled by adjusting the duration, temperature, and pressure during the reaction. This method, however, usually results in shorter products, which is rather unappealing [64,65].

2.3.2 Hydrodeoxygenation

The process of hydrodeoxygenation (HDO) of bio-based feedstock produces hydrocarbon fuels with the advantages of low density and viscosity, and simple blending with conventional fossil fuels. In this reaction that involves oxygen is removed from the substrate while hydrogen is present. It is possible to restrict chemical functions by removing the oxygen [63,66].

2.3.3 Decarboxylation and Decarbonylation

Decarbonylation and Decarboxylation (DCO), this method is more economical and energy-efficient than the HDO route, which eliminates the oxygen atom from fatty acids and esters by converting them into H_2O under the H_2 atmosphere. HDO process starts with the saturation of the double bonds C=C present in the alkyl chain followed by the cleavage of the C-O bond forming a fatty acid. This later undergoes further hydrogenation [67,68].

2.3.4 Hydrolysis

The hydrolysis of the ester is a chemical process in which a water molecule breaks a bond. To break the ester bond, water or a hydroxide ion typically assaults the carbonyl carbon of the ester group. To produce alcohol, one component of the original molecule absorbs the hydrogen ion from water. Meanwhile, the other fragment acquires the hydroxide group to produce a carboxylic acid salt (**Fig 2.2**).

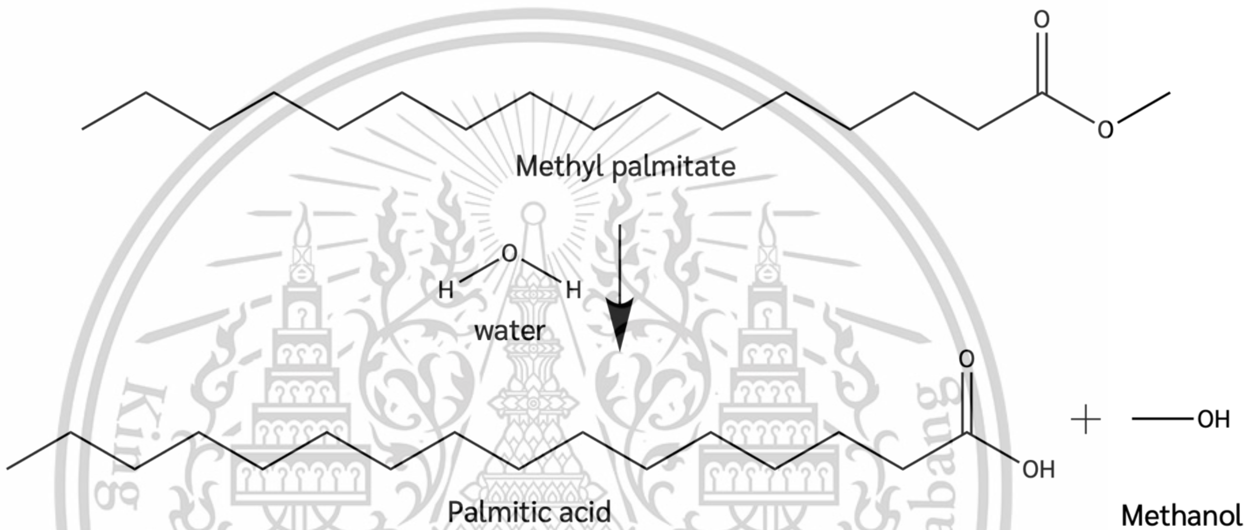

Fig 2.2 Hydrolysis of methyl palmitate to palmitic acid and methanol

Without the addition of a strong acid or base, only a few hydrolysis processes occur under normal circumstances. The strong acid or base works as a catalyst to speed up the process and is then recovered. The hydrolysis reaction can be reversed. A condensation process is so named because it generates water as a byproduct. One of the first instances of a hydrolysis reaction is the hydrolysis of a triglyceride (for example, to generate soap in a process known as "saponification") [69,70].

2.3.5 Ketonization

Ketonization is the process that occurs when two carboxylic acids combine to form a ketone, carbon dioxide, and water. This is shown using palmitic acid as an example in **Fig 2.3**. While this reaction was originally used in the manufacturing of acetone, it is now gaining popularity for its use in the upgrading of biomass-derived oxygenates. One example is the upgrading of bio-oil produced by rapid pyrolysis of biomass. The ketonization process is critical for reducing the negative effects of carboxylic acids in bio-oil. The oxygen vacancy sites, which are detailed in the next section, often accelerate ketonization [18,20].

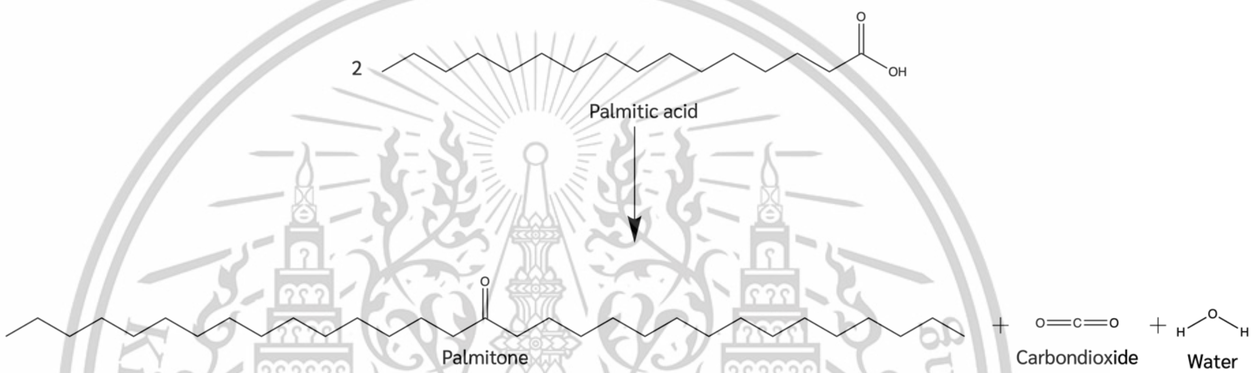

Fig 2.3 Ketonization reaction of palmitic acid to palmitone.

The ketonization mechanism on metal oxide surfaces without and with oxygen vacancies has been experimentally and theoretically studied. One such example is the ZrO_2 surface by the ß-ketoacid mechanism of acetic acid as shown in **Fig 2.4**. (Acetic acid was employed because the small size makes the calculation less time-consuming, but this equally applies to larger acids.) This comprises (a) acetic acid molecular adsorption, (b) enolate species formation, (c) acyl species creation, (d) C-C coupling of enolate and acyl species to generate a ß-ketoacid, and finally (e) acetone decarboxylation of ß-ketoacid. The production of acyl species on non-reduced ZrO_2 was shown to be unstable. However, the reduced ZrO_2 surface can stabilize an acyl species for further reaction with an enolate intermediary to generate ß-ketoacid. That is, in comparison to the stoichiometric ZrO_2 surface, a surface with surface oxygen vacancy enhances the synthesis of the ß-ketoacid [18]. demonstrates the beneficial effect of oxygen vacancy.

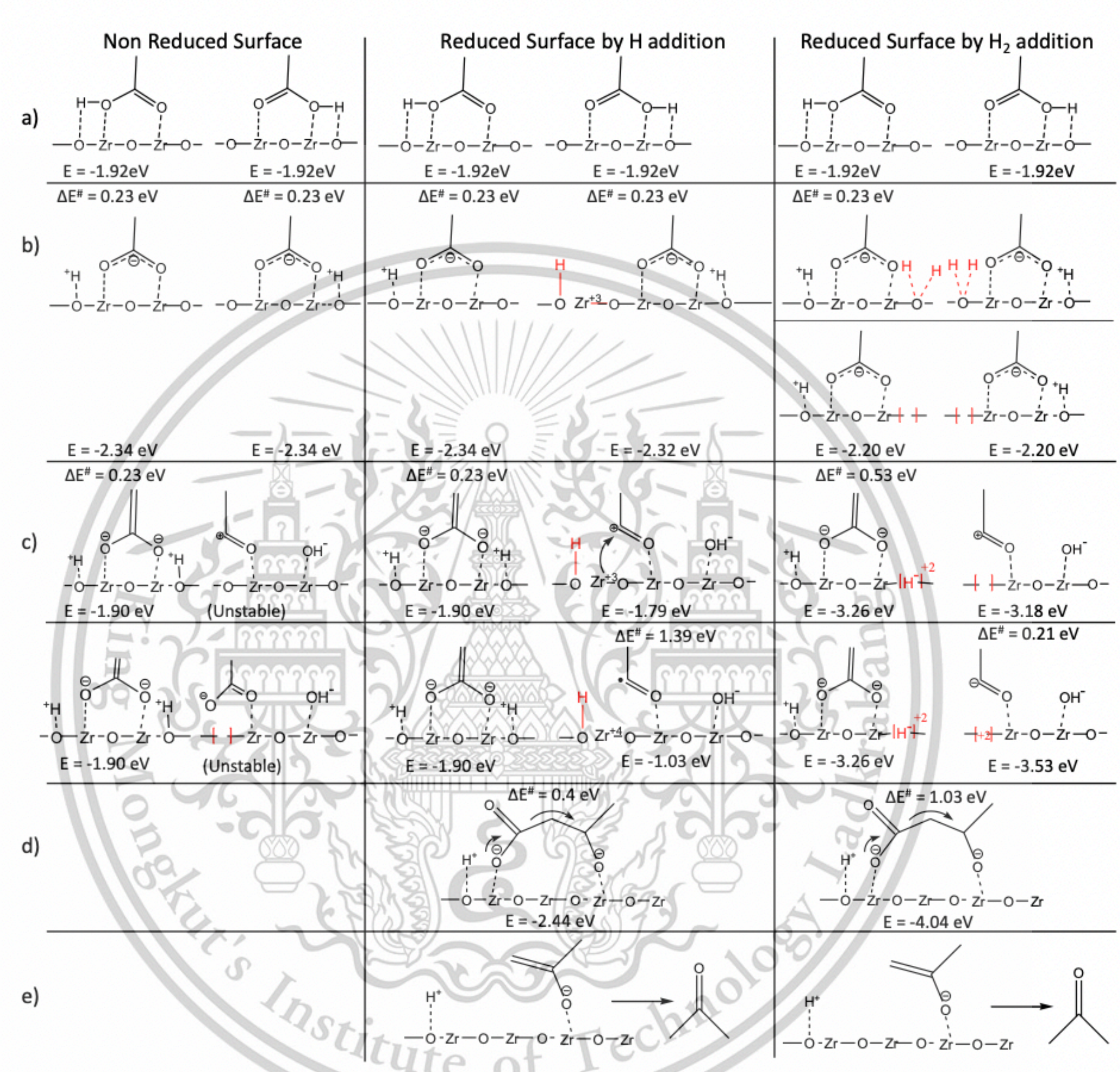

Fig 2.4 The interaction of acetic acid over non-reduced (left column) and reduced zirconia surface by hydrogenation (center column) and oxygen vacancy creation (right column) [18].

2.4 Titanium dioxide (TiO_2) as ketonization catalyst

Titanium dioxide (TiO_2) or titania is one of the most important semiconducting metal oxides. It is known to absorb UV light, have unique charge transport capabilities, and display surface adsorption. One of the most significant defects discovered in TiO_2 is oxygen vacancy. Anatase structure, one of the most prevalent TiO_2 polymorphs, is shown in **Fig 2.5**.

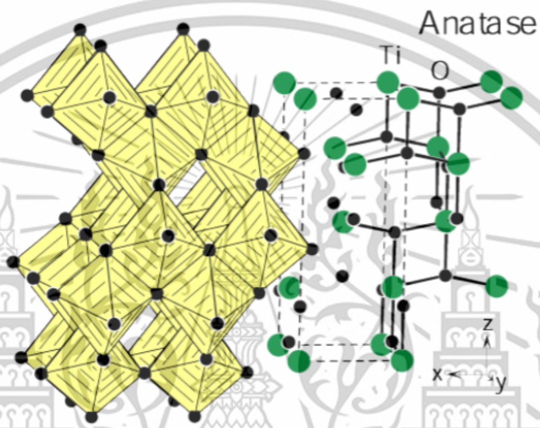

Fig 2.5 The crystal structure of anatase phase TiO_2 [71].

2.4.1 Oxygen vacancy or Lewis Ti^{3+} sites

Oxygen vacancy in metal oxides has been extensively investigated both by theoretical calculations and experimental characterizations. Oxygen vacancies are now widely regarded as significant adsorption and active sites for heterogeneous catalysis. This, in turn, has a significant impact on metal oxide reactivity, such as electronic structure, charge transport, and surface characteristics. When oxygen vacancy occurs on TiO_2, it produces unpaired electrons or Ti^{3+} centers. Ion sputtering, electron beam bombardment, thermal annealing in a controlled gas such as hydrogen, and low-intensity UV photon irradiation can all be used to achieve this. Annealing TiO_2 under varied circumstances can significantly change the defect concentration. **Fig 2.6** depicts the reduction of anatase-type TiO_2 by H_2 at temperatures ranging from 400 °C to 550 °C. in a temperature-programmed reduction (TPR) experiment to be discussed later. It is known that excess electrons on oxygen vacancy states influence the surface adsorption and reactivity of important adsorbates like O_2 or H_2O on the TiO_2 [72]. The oxygen vacancy also serves as a donor level in TiO_2's electronic structure. Furthermore, it influences the electron-hole recombination process in photocatalysis.

When metal is loaded onto the TiO_2 support, it was found that the reduction shifts to a lower temperature, indicating the facile generation of oxygen vacancy. This is shown in **Fig 2.6** using 10%Pd/TiO_2 as an example. This catalyst shows a peak of about 160 °C assigned to the strong metal-support interaction (SMSI) effect and another peak of about 420 °C assigned to the reduction of the TiO_2 surface. The observed decrease in TiO_2 reduction temperature from 530 to 420 °C in the presence of Pd is attributed to the interactions between Pd and TiO_2, which have also been observed for other noble metals. It has been suggested that the dissociation of hydrogen on the Pd particles and its subsequent spillover to TiO_2 leads to the lower reduction temperature of the latter [41]. This finding is not limited to Pd but extends to other catalysts as well as shown in **Table 2.4**.

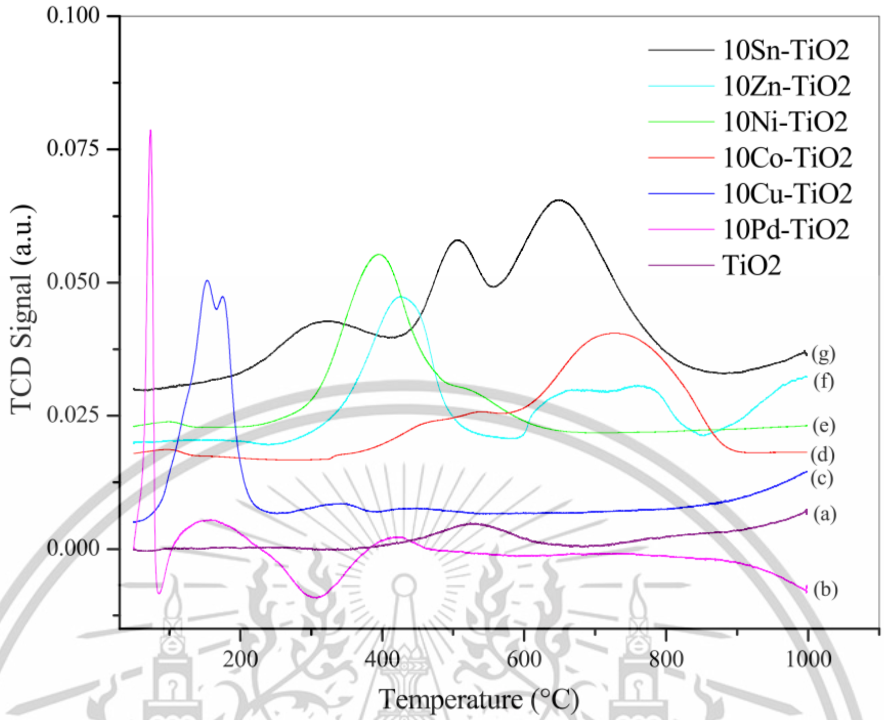

Fig 2.6 Temperature programmed reduction profiles of anatase TiO_2 and M/TIO_2 [41].

Table 2.3 Surface area, reduction temperature, and H_2 consumption of different M/TiO_2 catalysts.

Catalyst	Surface area (m^2/g)	Reduction temperature (°C)	H_2 consumption (mmol/g)	Ref.
TiO_2	147	550	-	[41]
10%Pd/TiO_2	100	160	-	[41]
1%Pt/ $K_2Ti_6O_{13}$	19	154	-	[73]
1.5%Ru/TiO_2	50	200	2.72	[74]
Ru/TiO_2	177	100	0.48	[75]
Pt/TiO_2	88	250	-	[76]

2.4.2 Hydrogen dissociation and spillover

Hydrogen dissociation and spillover describe the migration of H atoms from the metal particles to the support, *i.e.*, from a hydrogen-rich to a hydrogen-poor surface as shown in **Fig 2.7**. Spillover is widely defined as the movement of a species that has been adsorbed or created on one surface to another surface that does not adsorb this species under the same conditions. Only the overflow of catalytically active species is significant in catalysis. Hydrogen atoms are seldom formed on the surface of a support such as TiO_2 alone. In H_2 spillover, H atoms form on a metal surface and move to the surface of the support [42].

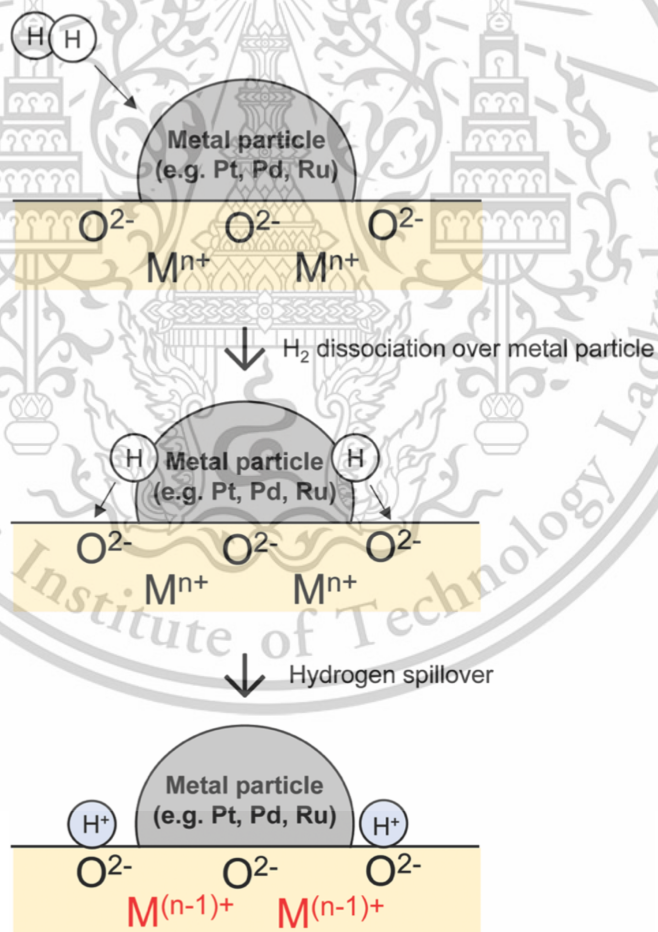

Fig 2.7 Spillover of H atoms from metal particles to reducible metal oxides [77].

When TiO_2 loaded with metal particles is exposed to H_2, the transmission of the IR spectrum decreases strongly due to the formation of a broad IR absorption band. This is explained by the transfer of H atoms from metal particles to TiO_2. On the surfaces of metal oxide, hydrogen atoms combine to create electrons and protons. Protons generate charge carriers by creating M-O(H)-M moieties that are bonded inside the crystal, while electrons are trapped at defect sites that are slightly below the conduction band edge. The absorption of IR light causes electronic excitation from these shallow traps into the conduction band, resulting in a high absorbance throughout the range of 1000-4000 cm^{-1} due to the delocalization of the excited electrons in the conduction band. As a result, this band is evidence of shallow defect sites formed by the reduction of Ti^{4+} cations by H atoms [78–80]. Typical noble metals such as Ru, Pt, and Pd, are used to promote the H_2 spillover on TiO_2 support. This is a summary of noble metal property

Platinum (Pt)

- Appearance: Soft, lustrous, silver-colored.
- Density: 21.5 g/cc (highly density).
- Malleability and Ductility: Very malleable and ductile (ongoing debate about its rank among the most ductile metals).
- Corrosion Resistance: Extremely resistant to corrosion.
- Boiling Point: Around 3825 °C.

Ruthenium (Ru)

- Appearance: Silvery whitish, lustrous, with a shiny surface.
- Density: 12.2 g/cm^3
- Hardness: Harder than platinum.
- Reactivity: Unreactive at room temperature, maintaining its luster, but exhibits paramagnetic behavior.
- Boiling Point: Around 4150 °C
- Reaction with Oxygen: Oxidizes when heated to around 800°C.

Palladium (Pd)

- Appearance: Precious gray-white metal, with a shiny surface.
- Density: 12.007 g/cm^3
- Ductility: Extremely ductile and easily worked.
- Corrosion Resistance: Not tarnished by the atmosphere at ordinary temperatures.
- Uses: Often used as a substitute for platinum in jewelry and electrical contacts; palladium leaf is used for decorative purposes.
- Boiling Point: Around 2963 °C.

2.5 Literature reviews

Lee *et al.* [17] investigated the effects of fatty acid structures on ketonization selectivity and catalyst deactivation. The authors showed that the production of fatty ketone steadily reduced with increasing unsaturation degree of the fatty acids. Meanwhile, the McLafferty rearrangement (i.e., cracking) produced byproducts such as methyl ketones and olefins. The ketonization of a saturated fatty acid produced a high fatty ketone yield (90%) with little deactivation. Unsaturated fatty ketone, on the other hand, deactivates quickly.

Promchana *et al.* [73] have performed mechanistic studies on the conversion of fatty acids to long-chain olefins using titanate-based catalysts, such as alkali hexatitanates $A_2Ti_6O_{13}$ (A = Li, Na, and K), $Na_2Ti_3O_7$, and $K_2Ti_4O_9$. The tunnel structure of $A_2Ti_6O_{13}$ was shown to be stiffer than that of layered $Na_2Ti_3O_7$ and $K_2Ti_4O_9$. Furthermore, these catalysts exhibit both reducibility and basic properties, but only the reducibility affects the long-chain olefin products.

Borja Oliver *et al.* [15] investigated the effect of temperature on ketonization. With methyl stearate as the substrate and ZrO_2 as the catalyst, nearly a 50% yield of linear C_{35}-waxes was obtained. As a byproduct, high-quality diesel with a high linear alkane concentration and near-zero oxygen content was achieved in more than 25% yield. When temperatures rise, the C_{35}-ketone product shrinks and transforms into a long-chain hydrocarbon.

Gianfranco *et al.* [29] found that the ease with which metal carboxylates form and their ability to decompose is an important descriptor for ketonization activity. Also, this is dependent on the nature of the doping metals, catalyst pretreatment, and reaction conditions. Recent investigations on the ketonization of simple carboxylic acids and aldehydes reveal that, as with mixed metal oxides, ketonization requires a balanced population of acid/basic site pairs (e.g., Al_2O_3, TiO_2, ZrO_2).

Rawesh Kumar *et al.* [18] investigated the mechanism of ketonization. It was found that neighboring adsorbed carboxylates, or a carboxylate and carboxylate moiety, react to create reaction intermediates (β-ketoacid) that convert to ketones. However, the mechanistic picture for the ketonization of aldehydes, alcohols, and esters is less clear. Nonetheless, surface carboxylate intermediates are formed from these feedstocks by processes such as aldehyde oxidation, ester hydrolysis, and the Cannizzaro reaction. In the case of ester, β-ketoester (similar to β-ketoacid) can arise by Claisen or Dieckmann condensations.

Guntida *et al.* [23] reported the importance of oxygen vacancies in palmitone selectivity and coke production over TiO_2, CeO_2, MnO_2, and ZrO_2 catalysts for methyl palmitate ketonization. The results demonstrated that oxygen vacancies might increase palmitone selectivity while trapping the hydrogen atom to prevent spillover.

Maluangnont *et al.* [27] reported the deoxygenation of palmitic acid into diesel-range hydrocarbon by ketonization and subsequent cracking of the produced ketone over CeO_2 catalysts. The nanocrystalline ceria catalyst was evaluated in a fixed-bed flow reactor at 400 °C with atmospheric N_2 or 10% H_2/N_2. The oxygen vacancies were discovered to be active in the ketonization of palmitic acid to C_{31}-ketone and subsequent cracking. A C_9 to C_{17} liquid hydrocarbon selectivity of 22-27% was found at 100% palmitic acid conversion.

The measured yields of C_{17}-range ketones and hydrocarbons showed that the primary reaction process was ketone cracking. By maintaining the reduced surface using H_2 carrier gas, ketonization and cracking activity were enhanced.

Catalytic ketonization of palmitic acid over a series of transition metal oxides supported on zirconia oxide-based catalysts has been reported by A. Aleem et al [24]. Under optimal conditions of 3 h, 340 °C, and 5% loading MnO_2 over ZrO_2, 16-hentriacontanone was the main product, and pentadecane as a byproduct. This catalyst converted 92.3% of palmitic acid while yielding 27.7% and 10.8% of 16-hentriacontanone and pentadecane, respectively.

Aside from the more common anatase (or rutile) TiO_2, there are a few works on the reducibility and production of oxygen vacancy sites in layered/tunneled titanates. According to Jinmeng et al [81], Pt/$K_2Ti_6O_{13}$ nanowire may be readily reduced due to the strong metal support interaction (SMSI), which increases coverage via H_2 spillover. This is consistent with the work by Promchana et al [73].

TiO_2 reducibility and the formation of an oxygen vacancy site or Ti^{3+} defect are well established. Tu et al [39]. investigated the reaction kinetics and mechanisms of aliphatic carboxylic acid ketonization over a Ru/TiO_2 catalyst. While Ru is inert for carboxylic acid ketonization, it promotes the reduction of titanium(IV) oxide to Ti^{3+} species, which supplies the active sites. A bimolecular reaction involving carboxylic acids (adsorbed in a bidentate-bridging mode) is proposed, which progresses via the ß-ketoacid intermediate.

Chapter 3

Research methodology

3.1 Reagents

Details on the reagents used in this research are summarized in Table 3.1.

Table 3.1 A list of reagents.

Chemical	Grade of purity	Manufacturer
Anatase titanium dioxide (TiO_2)	99.80%	CARLO ERBA
Air zero gas	99.99%	PRAXAIR
Hydrogen gas	99.99%	PRAXAIR
Hydrogen in Argon gas	10%	PRAXAIR
Chlorobenzene	99.5%	CARLO ERBA
Methyl palmitate	97%	SIGMA-ALDRIC
n-Dodecane	99.99%	THERMO SCIENTIFIC
Ruthenium chloride ($RuCl_3$)	100%	ALDRICH
Helium gas	99.99%	PRAXAIR
Nitrogen gas	99.99%	PRAXAIR
Chloroplatinic acid (H_2PtCl_6)	100%	ALDRICH
Palladium chloride ($PdCl_2$)	97%	SIGMA-ALDRIC
Titanium butoxide ($Ti(OBu)_4$)	99.5%	CARLO ERBA
Absolute ethanol anhydrous	99.99%	CARLO ERBA

3.2 Apparatuses

3.2.1. Glass bead

3.2.2. Glass wool

3.2.3. Glass syringe, SGE Analytical Science

3.2.4. GC needle, SGE Analytical Science

3.2.5. Graduate pipette and bulb

3.2.6 Laboratory glassware

3.2.7. Stirrer and heater

3.2.8. Protector laboratory hood, Science Technology

3.2.9. Quartz wool

3.2.10. Quartz tube

3.2.11. Furnace, Utsakan No. SCG-14

3.2.12. Powder X-ray diffractometer

3.2.13. Gas chromatography, Agilent Technologies 7890B, Varian 3800 14. Vacuum pump

3.2.14 Borosilicate glass tube

3.2.15 Glass rod

3.2.16 Saturator

3.2.17 Syringe pump

3.2.18 Surface area and pore size analyzer, Autosorb-1, Quantachrome

3.2.19 Alumina crucible

3.2.20 Agate mortar

3.2.21 Thermogravimetric analyzer, Pyris, Perkin Elmer

3.2.22 Gas chromatography, Varian 3800

3.3 Catalyst preparation

3.3.1 Impregnation method

The incorporation of ~0.5 wt% noble metals (Pt, Pd, and Ru) on TiO_2 was prepared by the impregnation method. For 0.5Pd/TiO_2, 20 g of the commercially available TiO_2 was dried in an oven at 60 °C for 1 h. Meanwhile, 0.1675 g of $PdCl_3$ was dissolved in 20 mL of distilled water. This solution (5 mL) was slowly added dropwise onto the TiO_2 support with intermediate drying in an oven at 60 °C for 30 min. This was repeated until a total of 20 mL of the solution was employed. Finally, the solid was calcined at 450 °C for 10 h under air using a heating rate of 3 °C/min. 0.5Ru/TiO_2 and 0.5Pt/TiO_2 catalysts were prepared with the same procedure.

3.3.2 Sol-gel method

For the comparative study between commercial TiO_2 and synthesized TiO_2 by sol-gel method was synthesized according to Dubey et al [82]. For the sol-gel process, 150 mL ethanol was mixed with 10 mL deionized water under constant stirring at 65 °C. Further, 9 mL titanium butoxide ($Ti(OBu)_4$) was added to the above solution and the mixture was heated to 85 °C for another 5 h. After that, the mixture was cooled down to room temperature and then filtered. The solid gel was dried at 60 °C overnight and then calcined at 450 °C for 10 h.

3.4 Catalysts characterization

3.4.1 X-ray diffraction (XRD)

The crystalline phase of the catalysts can be identified using powder X-ray diffraction (XRD). The sample was ground before it was packed on the sample holder. Analysis was done employing Bruker diffractometer (CuK_α radiation, 40 kV, 30 mA), covering the range 2θ = 5-65°, at the rate of 0.02°/step and a scanning rate of 0.6 s/step.

The samples characterized included as received/as made, post-TPR, and all spent samples.

3.4.2 Temperature-programmed reduction (H_2-TPR)

The amount of oxygen vacancy site including its strength can be determined by a temperature-programmed reduction by H_2 gas (H_2-TPR). The measurement was performed in a quartz tube connected with a thermal conductivity detector (VICI). Prior to an analysis, the sample (0.2 g approximately) was activated in the air (flow rate of 30 mL/min) from room temperature to 400 °C at a heating rate of 10 °C/min followed by an isothermal treatment at 400 °C for 30 min. Subsequently, the system was naturally cooled down in the atmosphere of nitrogen gas (flow rate of 30 mL/min) to room temperature. Then, the temperature reduction profile was recorded under 10% H_2/Ar at the heating rate of 10 °C/min, from 50 to 900 °C, with holding at 900 °C for 5 min. The TCD signal was calibrated employing a known mass of CuO as a standard, considering that CuO is reduced stoichiometrically and completely to Cu and H_2O. The reduction profile of CuO and the calculation of the hydrogen consumption can be found in **Appendix A**. The amount of oxygen vacancy sites is expressed as mmol of H_2 consumed per mass of a catalyst (mmol H_2/g).

3.4.3 Temperature-programmed desorption (NH_3-TPD)

The amount and strength of acid sites can be determined by a temperature-programmed deduction by NH_3 gas (NH_3-TPD). The measurement was performed in a quartz tube connected with a thermal conductivity detector (VICI). Prior to an analysis, the sample (0.2 g approximately) was activated in the air (flow rate of 30 mL/min) from room temperature to 400 °C at a heating rate of 10 °C /min followed by an isothermal treatment at 400 °C for 1h. Subsequently, the system was naturally cooled down in the atmosphere of nitrogen gas (flow rate of 30 mL/min) to room temperature. Then, reduction in H_2 (flow rate of 30 mL/min) from room temperature to 400 °C at a heating rate of 10 °C /min followed by an isothermal treatment at 400 °C for 2h. Subsequently, the system was naturally cooled down in the atmosphere of nitrogen gas (flow rate of 30 mL/min). The NH_3 adsorption (flow rate of 30 mL/min) was performed at room temperature for 1 h, and the catalyst was flushed by He gas for 1 h. Then, the temperature desorption profile was recorded under He at the heating rate of 10 °C/min, from 50 to 400 °C, with holding at 400 °C for 2 h. The TCD signal was calibrated employing a known mass of NH_3 zeolite Y as a standard. The amount of acid sites is expressed as mmol of NH_3 consumed per mass of a catalyst (mmol NH_3/g).

3.4.4 Surface area measurement (BET)

A gas adsorption analyzer can determine the surface area of the catalysts (Autosorb-1C, Quantachrome). An amount of 0.05 g of the sample was put into the cell, which was connected to the outgassing station. During the outgassing process, the temperature was increased to 300 °C. Following that, nitrogen gas was supplied into the sample cell, where adsorption could be evaluated throughout a partial pressure (P/P_0) range of 10^{-6} to 1.0. The adsorption isotherm and surface area were calculated using the BET equation, as stated in Equation 3.1.

$$\frac{1}{\upsilon\left[\left(\frac{P_0}{P}\right)-1\right]}=\frac{c-1}{\upsilon_m c}\left(\frac{P}{P_0}\right)+\frac{1}{\upsilon_m c} \qquad \text{Equation 3.1}$$

where P and P_0 are the equilibrium and the saturation pressure of adsorbents at the temperature, υ is the quantity of monolayer adsorbed gas, and *c* is the BET constant. The theory's concept is an extension of the Langmuir theory, which is a theory for monolayer molecular adsorption to multilayer adsorption with the following hypotheses:

(a) gas molecules physically adsorb on a solid in infinite layers; (b) there is no interaction between each adsorption layer; and (c) the Langmuir theory can be applied to each layer.

3.4.5 Raman spectroscopy

The sample, as made or spent, was finely ground. It was then packed into a sample holder. Raman spectra were recorded using a DXR Smart Raman (Thermoscientific) at the laser wavelength of 532 nm and the laser power of 5 mW. This allows the quick determination of the relative content of coke.

3.4.6 Diffuse reflectance UV-VIS spectrophotometer (DR-UV)

The sample 0.1 g was mixed and ground in the crystal of barium sulfate (~1g) for dilution. It was subsequently pressed on the sample holder, covered by a quartz slide, and measured on a UV-VIS spectrometer, T92+, PG instruments using boric acid for a baseline correction. The spectra were collected from the range of 200-800 nm.

3.4.7 Inductively coupled plasma – Optical emission spectrometry (ICP-OES)

An amount of ~0.1 g of sample was digested in HNO_3/H_2SO_4 (1:2 by volume). The solution was diluted with DI water and analyzed by Inductively coupled plasma-optical emission spectrometry (ICP-OES) using an Avic 550 Max, PerkinElmer instrument.

3.4.8 Transmission electron microscope (TEM)

The samples were prepared by drop-casting of aqueous dispersions of oct, DODA-oct, and 4CzIPN/DODA-oct onto a carbon-coated Cu grid with a 200 mesh. The grids with dispersions were dried in air to remove the solvent overnight in the dark.

3.4.9 X-ray photoelectron spectroscopy (XPS)

X-ray photoelectron spectroscopy (XPS) was performed to investigate the oxygen vacancies (Ov), sub-oxide (Os), and the oxidation state of Ti over the catalysts. The XPS spectra were obtained by AMICUS spectrometer using MgKα X-ray radiation and AlKα X-ray radiation at a voltage of 15 kV and current of 12 mA.

3.5 Catalytic testing

The catalytic activity was carried out in a fixed-bed gas flow reactor as shown in **Scheme 1**. Before the reaction, the catalyst was activated under air-zero at 400 °C (flow rate of 60 mL/min) for 1 h. Subsequently, it was reduced under H_2 (flow rate of 60 mL/min) at 400 °C for 2 h. The temperature was held at 400 °C under H_2 (flow rate 50 mL/min) and the ketonization was performed by injecting methyl palmitate in n-dodecane (10% and 20% w/v) with a rate of 3.1 mL/h (0.977 mmol/h) (contact time 58-581 gh/mol see **Appendix B**). In the reaction under N_2, the carrier gas was switched to N_2 (flow rate 50 mL/min) before feed injection. The reactor outlet was heated at 120 °C by a heating tape to maintain the product as a liquid. The product was trapped by 5 mL of chlorobenzene and analyzed using an offline GC-FID with HP- 5MS column (Varian 3800, 30 m x 320 μm x 0.25 μm). The gas product was analyzed using online gas chromatography equipped with a thermal conductivity detector (TCD) using a PoraPLOT Q-HT column (Agilent 6890, 27.5m x 0.32 mm x 10 μm). For the reaction in the presence of water vapor, the carrier gas was flown to a water-filled saturator at room temperature. Examples of the chromatograms are shown in **Appendix C**.

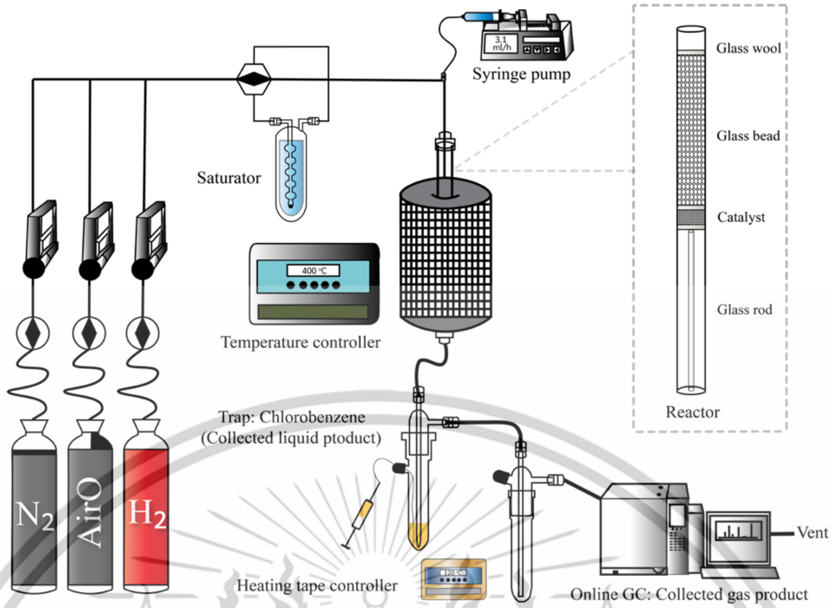

Scheme 1 Schematic diagram of the catalytic testing rig.

Chapter 4

Main results and discussion

4.1 Catalyst characteristics

Elemental compositions and specific surface areas of catalysts determined by N_2 adsorption-desorption are shown in **Table 4.1**. The metal loadings on TiO_2 support were obtained as expected from the designated value (~0.5 wt%). After the metal was incorporated, the surface areas of the catalyst slightly decreased from the parent anatase TiO_2 (from 60 to 45-55 m^2/g) suggesting a high metal dispersion over the TiO_2 support. In line with this view, the diffraction pattern of metal oxide or metal cannot be observed in XRD (**Fig. 4.1**). Only peaks at 2θ = 24.8˚, 37.3˚, 47.6˚, 53.5˚, 59.1˚, 69.5˚ of TiO_2-anatase phase [83] were observed and retained after metal loading. This suggested no phase transformation of anatase to rutile/brookite [84] upon calcination and metal doping. It is worth noting that the decrease in XRD intensity for the metal-loaded catalysts is presumably due to the X-ray absorption by the incorporated metals.

Table 4.1 Physicochemical properties, surface composition, and acidity of the reduced TiO_2-based catalysts.

Entry	Catalyst	Surface area^a (m^2/g)	Metal loading^b (%)	H_2-consumption^c (mmol/g)	Surface Ti^{3+}/(Ti^{3+} + Ti^{4+})^d	%Surface oxygen vacancy^d	Band gap^e (eV)	Total acidity^f (μmol/g)
1	**TiO_2**	60	-	0.30	0.02	26	3.16	10.5
2	**0.5Pt/TiO_2**	60	0.4	1.94	0.05	41	3.10	8.9
3	**0.5Ru/TiO_2**	45	0.4	1.45	0.05	43	3.03	12.2
4	**0.5Pd/TiO_2**	54	0.5	1.41	0.10	45	3.00	14.8

^{a}BET, ^{b}ICP, ^{c}H_2-TPR, ^{d}XPS, ^{e}DR-UV, ^{f}NH_3-TPD

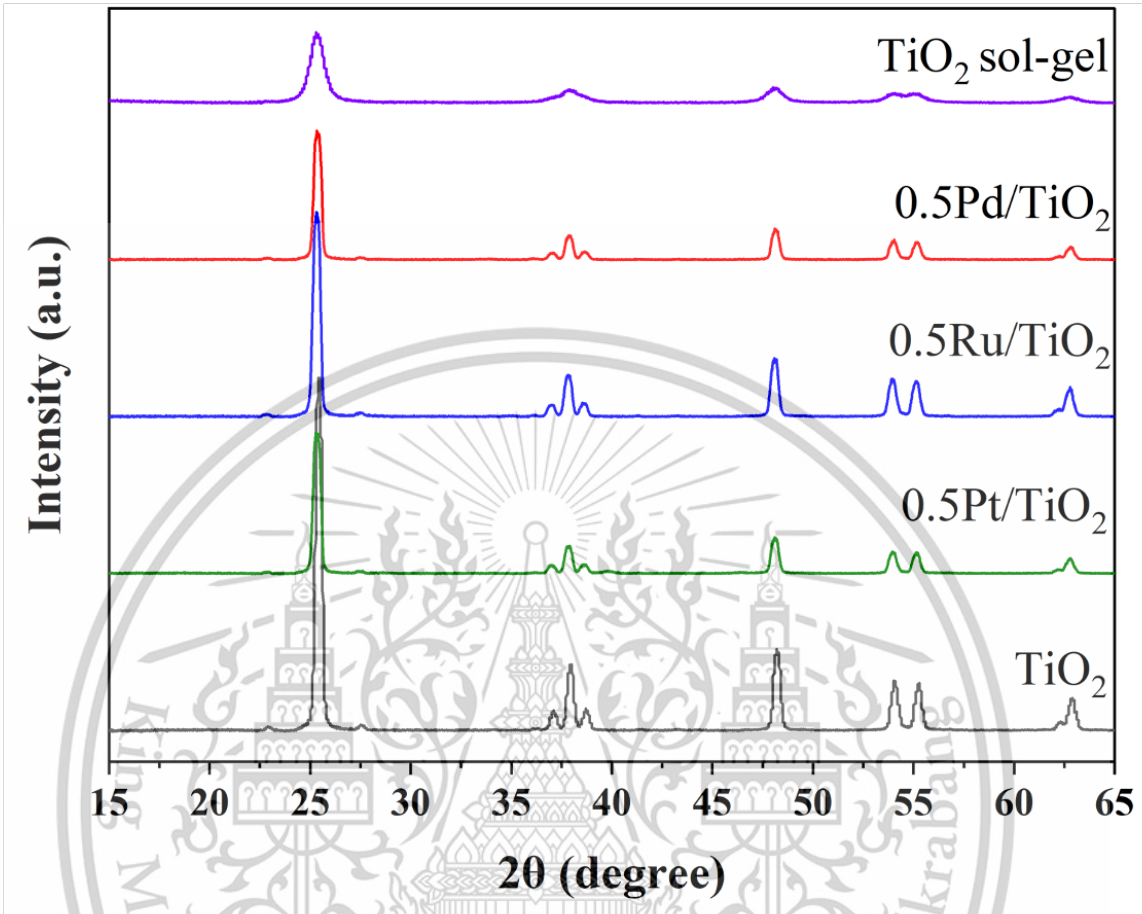

Fig 4.1 The X-ray diffraction patterns of the catalysts

The metal dispersion was evidenced by the TEM image and elemental mapping in **Fig. 4.2**. A larger Pt particle size of 19 ±9 nm, compared to a smaller Pd and Ru particle size of 6 ±3 nm and 9 ±4 nm, was observed. Generally, higher metal dispersion could affect the formation of oxygen vacancy and Ti^{3+} sites upon the reduction. In support of this view, the H_2-TPR profile of metal-loaded TiO_2 (**Fig. 4.3**) showed a consecutive reduction of TiO_2 along with the corresponding metal, at the temperatures (~100-300 °C) lower than that of the TiO_2 support alone (~460-700 °C). Moreover, the total H_2 consumption for 0.5Pt/TiO_2 (1.94 mmol/g), 0.5Ru/TiO_2 (1.45 mmol/g), and 0.5Pd/TiO_2 (1.41 mmol/g) is higher than the expected metal content (0.5% loading, ~0.1-0.35 mmol/g). The observed lower reduction temperature of TiO_2 and excessive H_2 consumption indicates an H_2-spillover of the loaded metal that facilitates the reduction of the TiO_2 support to form Ti^{3+} and oxygen vacancy [85].

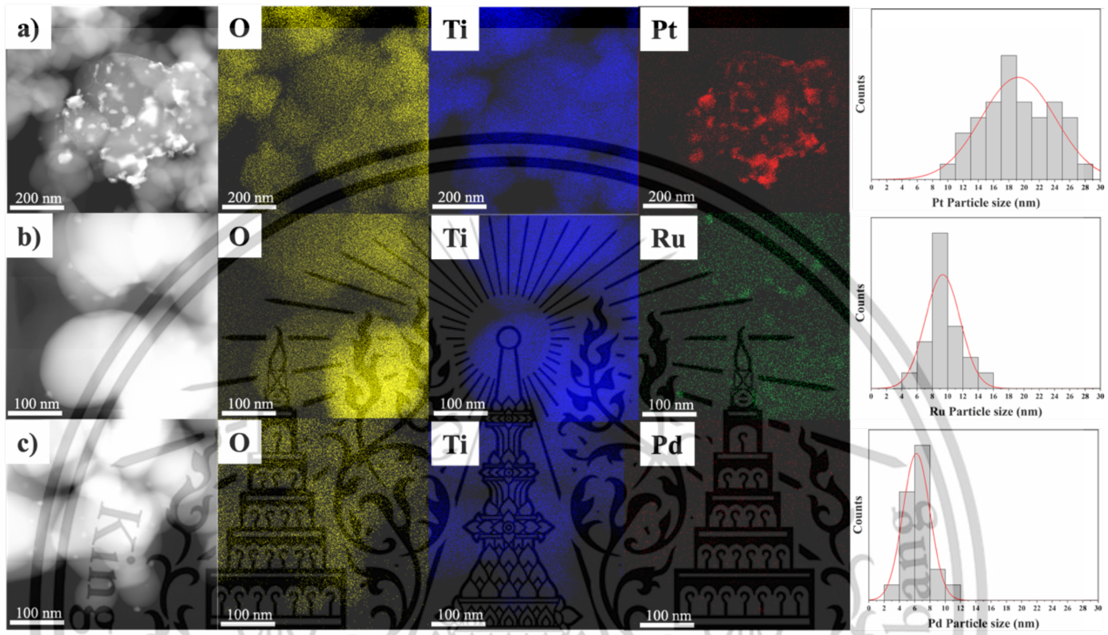

Fig 4.2 TEM-EDX of catalysts A) 0.5Pt/TiO_2, B) 0.5Ru/TiO_2, C) 0.5Pd/TiO_2

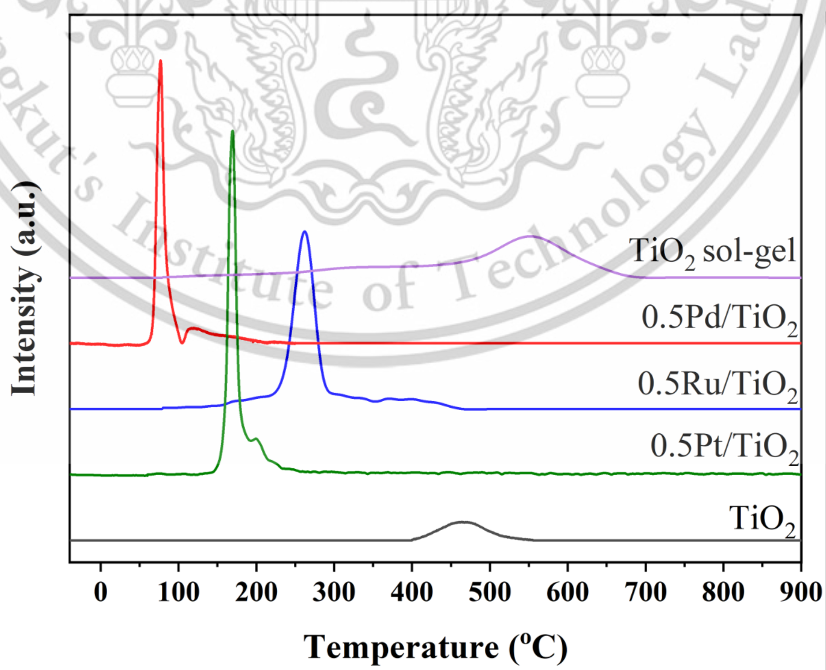

Fig 4.3 H_2-TPR profiles of the TiO_2 and metal incorporated TiO_2 catalysts

The Ti^{3+} and the oxygen vacancies can be observed by Ti2p and O1s XPS spectra shown in **Fig. 4.4**. The binding energy of Ti^{4+} peaks remained at 459.6 and 465.4 eV for the metals incorporated catalysts, except the 0.5Pt/TiO_2 (**Fig. 4.4a)**. The red shift of 0.3 eV (~459.3 and 465.1 eV) for 0.5Pt/TiO_2 may well derive from the higher electron-donating ability of Pt that would increase the electron density around the Ti center. After deconvolution, the Ti2p spectra show overlapping Ti^{3+} peaks at ~456.9 and ~462.7 eV, within the main Ti^{4+} peaks. The Ti^{3+} content can be calculated from the total area of Ti^{3+} divided by the total area of Ti^{3+} and Ti^{4+}, as expressed by "Surface $Ti^{3+}/(Ti^{3+} + Ti^{4+})$" shown in **Table 4.1**. The Ti^{3+} contents of the metals containing catalysts, particularly the 0.5Pd/TiO_2, are higher than that of TiO_2 support, presumably due to the improved H_2-dissociation and spillover, as discussed earlier.

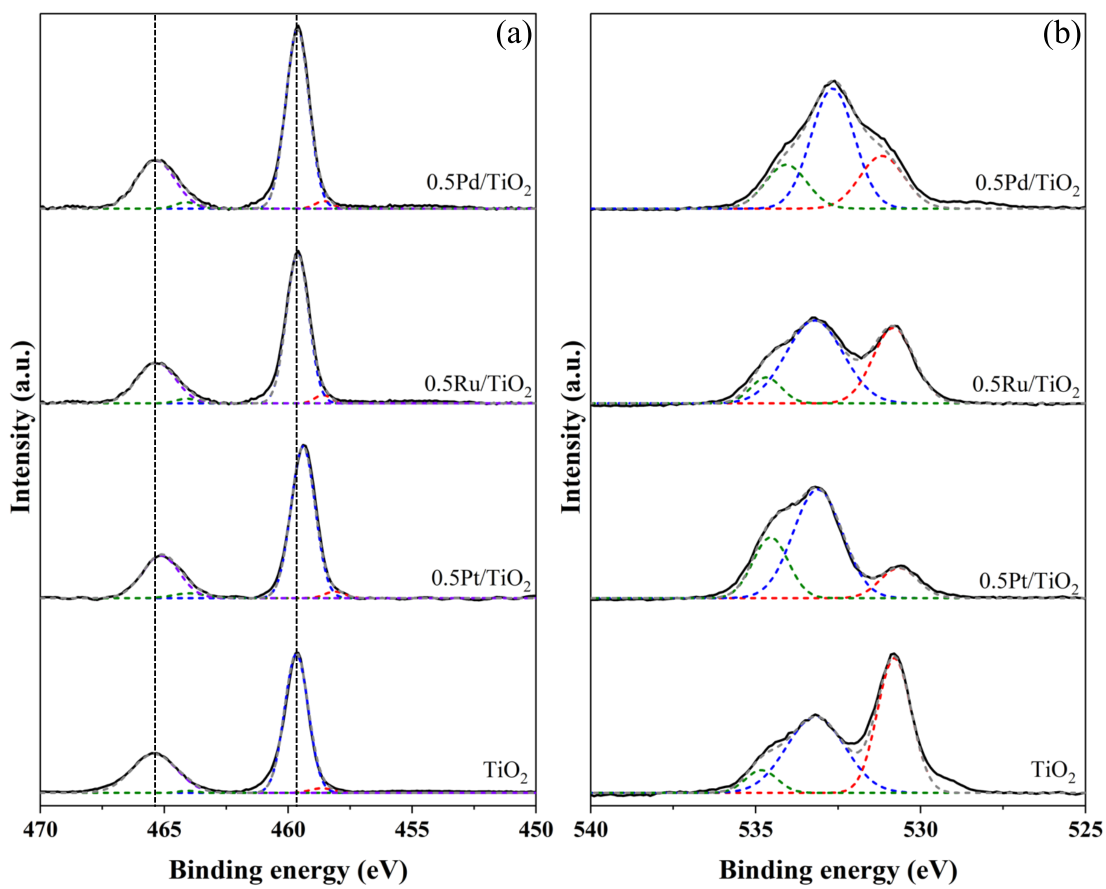

Fig 4.4 Ti2p XPS spectra (a) and O1s XPS spectra (b) of reduced catalysts

In a supportive manner, the deconvoluted O1s spectra (**Fig. 4.4b**) consist of three peaks at ~530.7, 533.2, 534.8 eV assigned to lattice oxygen (O_L), oxygen vacancy (O_v), and sub oxide (O_s), respectively [23]. The oxygen vacancies (O_v) notably increased from ~25% to ~40% when metals, i.e. Pd, were incorporated (**Table 4.1**). Although DR-UV spectra of all samples exhibited similar TiO_2 d-d transition in tetrahedral (~330 nm) and octahedral structure (~275 nm, **Fig. 4.5a**), slightly smaller energy band gaps of metals incorporated TiO_2 were evidenced (~3.0-3.1 eV, **Table 4.1** and **Fig. 4.6**). As compared to typical TiO_2 (3.20 eV) [86,87]), the lower energy band gaps indicate an increase in localized states of Ti^{3+} of metals incorporated TiO_2, especially for the 0.5Pd/TiO_2 sample.

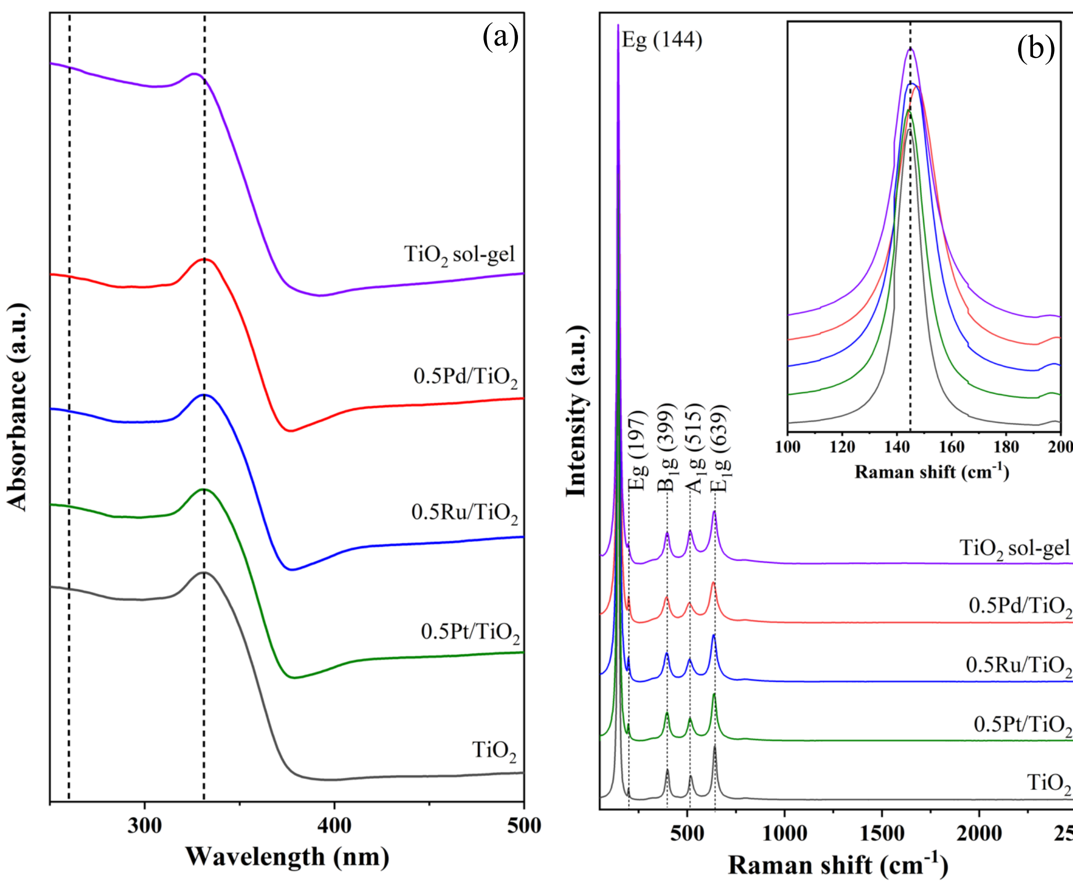

Fig 4.5 DR-UV spectra (a) and Raman spectra (b) of reduced catalysts

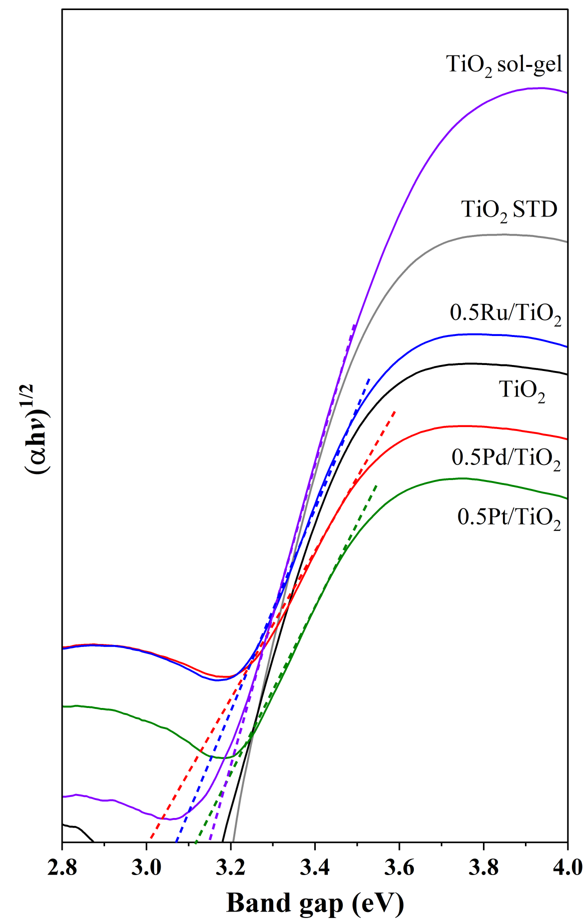

Fig 4.6 Tauc plot of reduced catalysts

Moreover, Raman spectra also showed peaks at 144, 197, 399, 515, and 639 cm^{-1} of O-Ti-O bond vibration modes of E_g, E_g, B_{1g}, A_{1g}, and E_g in anatase TiO_2 (**Fig. 4.5b**). This result corresponded to an O-Ti-O bond distortion due to the formation of O_v sites. A higher blue shift in the Raman spectra of 0.5Pd/TiO_2 (147 cm^{-1}) indicated a higher O_v site compared to 0.5Ru/TiO_2 (145 cm^{-1}), and 0.5Pt/TiO_2 (144 cm^{-1}) [87,88]. As the reduction by H_2 can generate oxygen vacancy and exposed Ti^{3+} sites (defect sites), an overall acid property of the catalyst can be modified. The more the Ti^{3+} sites, the more the total acidity, as evidenced by NH_3-TPD (**Fig. 4.7**). This is because the Ti^{3+} site acts as a Lewis acid site on the reduced surface. However, in the case of 0.5Pt/TiO_2, the higher electron donating ability of the incorporated Pt, as evidenced by the red shift in Ti2P XPS (**Fig. 4.4**), suppresses the Lewis acidity of Ti^{3+}. This would lead to lower total acidity of this sample

(8.90 mmol NH_3/g, 0.09 Ti^{3+}, **Table 4.1**) despite the high Ti^{3+} site as compared to TiO_2 alone (10.5 mmol NH_3/g, 0.07 Ti^{3+}). Accordingly, similar Raman spectra of 0.5Pt/TiO_2 and TiO_2 were observed (**Fig 4.5b**).

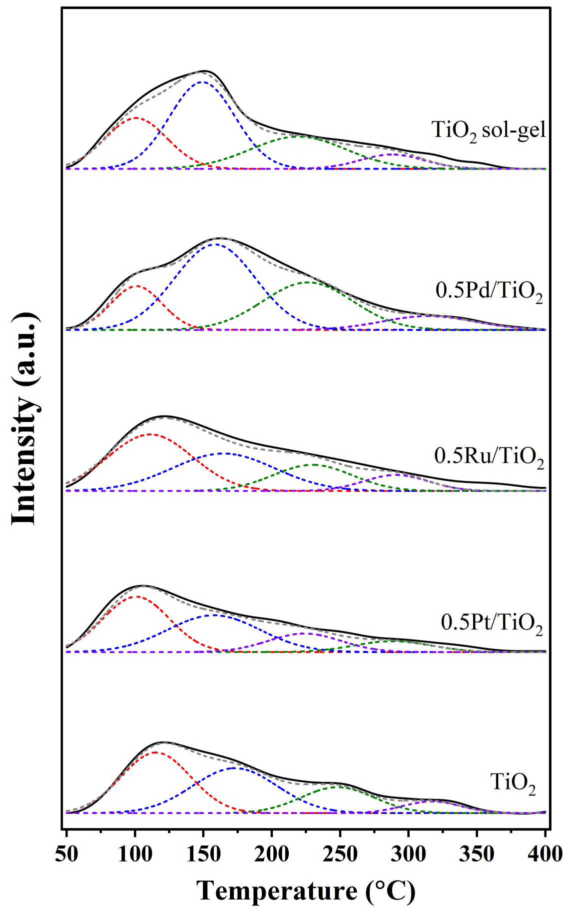

Fig 4.7 NH_3-TPD of reduced catalysts

4.2 Catalytic activity

4.2.1 Effect of water and carrier gas

The conversion of methyl palmitate over TiO_2 under various conditions was in the range of 57-94% and product distributions after ketonization are summarized in **Table 4.2**. The result showed that with water co-fed under N_2, the palmitone yield (70%) was higher than that without water co-fed (23%). This is because water could possibly activate the hydrolysis of methyl palmitate to palmitic acid over available acid sites (as in **Table 4.1**) as proposed in **Scheme 2**. Ketonization of the palmitic acid produced would be more readily promoted as compared to that of the parent ester [20]. Moreover, the presence of water suppresses deoxygenation since the palmitic acid produced, can undergo only decarboxylation to C15 alkane, while decarbonylation to C15 olefinic hydrocarbons is unlikely. This leads to a decrease in the selectivity of C15-C16 hydrocarbons from 10.5% to 4.0%. Hence, the subsequent cracking of the long chain olefins to C13-14 hydrocarbons would also decrease from 4.0% to 2.5% selectivity. While McLafferty rearrangement of the palmitone depends upon the level of conversion[27,89]. Therefore, the yield of C17 and C29 ketones increased from 1.4% to 2.8%. when water is present with the feed.

Table 4.2 Product distributions after ketonization of methyl palmitate over TiO_2 at 400 °C, at 2 hours on stream, W/F = 581 g.h/mol.

Water partial pressure (atm)	Carrier gas	Conversion (%)	%Yield (%Selectivity)					
			Palmitone	C15-C16 H/C	C13-C14 H/C	C17 and C29 ketone	CO	CO_2
-	N_2	57	23.0 (40.0)	6.0 (10.5)	2.3 (4.0)	1.4 (2.4)	1.3 (2.3)	2.2 (3.9)
0.24	N_2	90	70.0 (78.0)	3.6 (4.0)	2.3 (2.5)	2.8 (3.1)	3.0 (3.3)	7.3 (8.1)
0.24	H_2	94	74.0 (79.0)	4.3 (4.6)	1.9 (2.0)	3.2 (3.4)	2.3 (2.4)	7.8 (8.3)

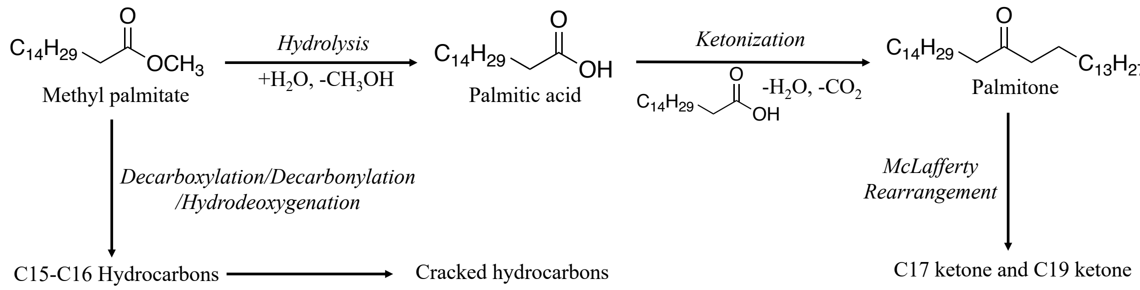

Scheme 2 Proposed reaction pathway for ketonization of methyl palmitate.

In addition, the stability was also improved with the addition of water as shown in **Fig. 4.8**. The reaction under N_2 without water co-feeding (**Fig. 4.8a**) showed a severe deactivation rate with time on stream. This is presumably because methyl palmitate strongly adsorbs on the surface, but the rate of ketonization of an ester is relatively slow[20,38,90]. Hence, the available active sites are gradually occupied by the methyl palmitate being fed. In other words, the active site is titrated by the feed as seen in **Fig. 4.9**. As the mole of methyl palmitate/mole of TiO_2 increased with feeding time (1 to 4 hours on stream), the mole of methyl palmitate converted/mole of TiO_2 was linearly decreased. An initial active site available can be roughly estimated from the intercept of methyl palmitate converted/mole of TiO_2 (~0.15 mole/TiO_2).

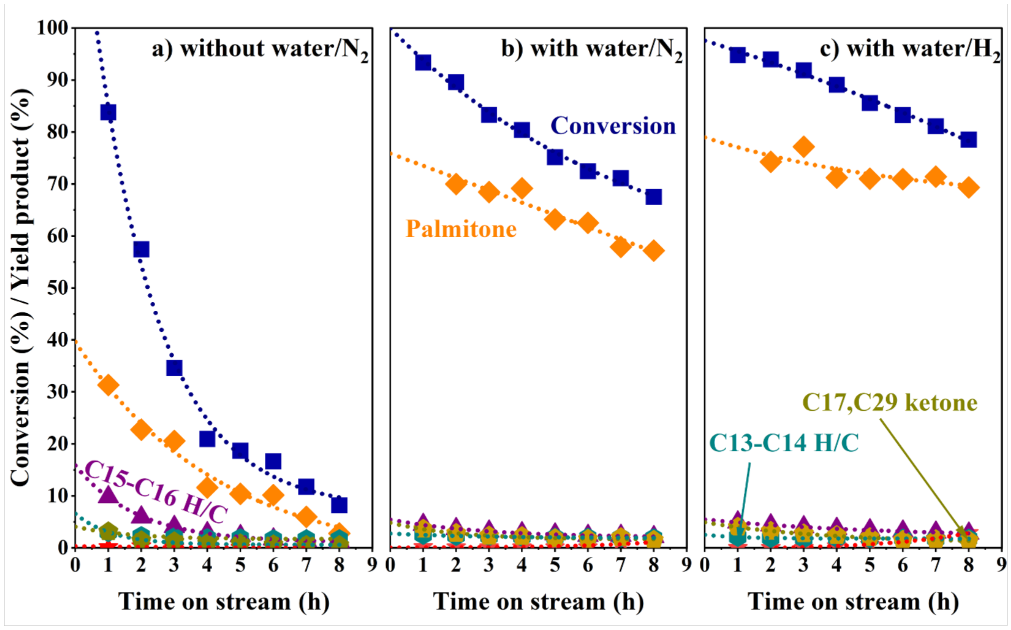

Fig 4.8 Effect of water and carrier gas on ketonization of methyl palmitate over TiO_2 (a) without water/N_2, (b) with water/N_2 (c) with water/H_2

Reaction condition 10% methyl palmitate in dodecane: 3.1 mL/h, N_2 or H_2 flow rate: 50 mL/min, contact time: 581 g.h/mol, activation temperature: 400 ℃ in air, reduction temperature: 400 ℃ under H_2, reaction temperature: 400 ℃, water: feed ratio 0 or 0.24.

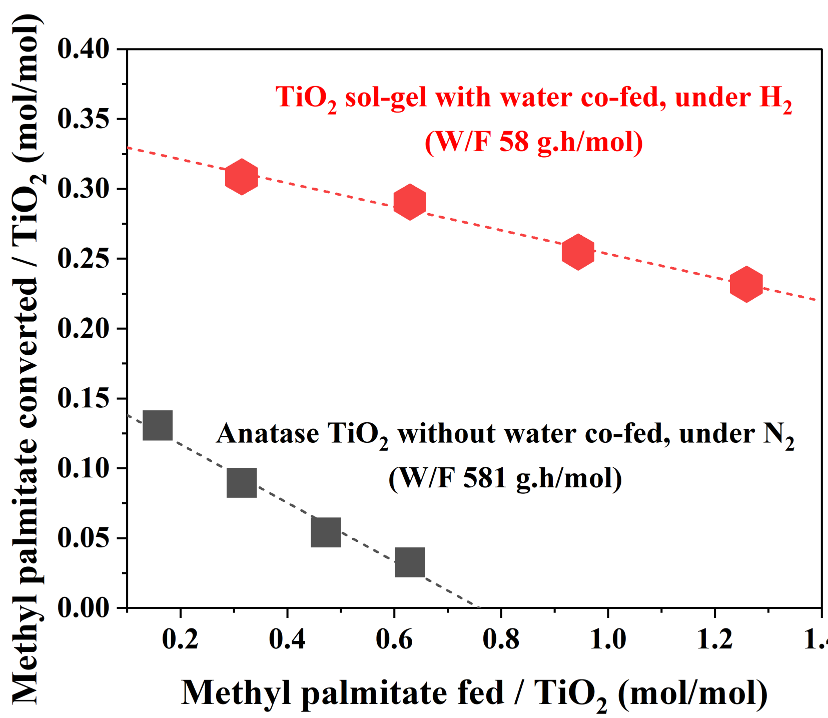

Fig 4.9 Methyl palmitate converted vs fed per mole of TiO_2 in the catalyst bed

In sharp contrast, a lower deactivation was observed for the reaction with water co-feeding (**Fig. 4.8b**). This is because the methyl palmitate can be converted to palmitic acid which is readily active for the ketonization, as discussed earlier. Moreover, TGA shows a mass loss of less than 3% and lower decomposition temperature of carbon deposit in the reaction with water co-fed, as compared to that under N_2 alone (**Fig. 4.10**). It is also worth noting that the initial palmitone yield was higher for the reaction with water co-fed (~75% *vs* ~40%, **Fig. 4.8b** *vs* **4.8a**). The higher initial activity could be derived from a decrease in TiO_2 crystallite size (i.e., higher surface area) when water is present, as evidenced by the XRD of the spent catalyst in **Fig. 4.11**.

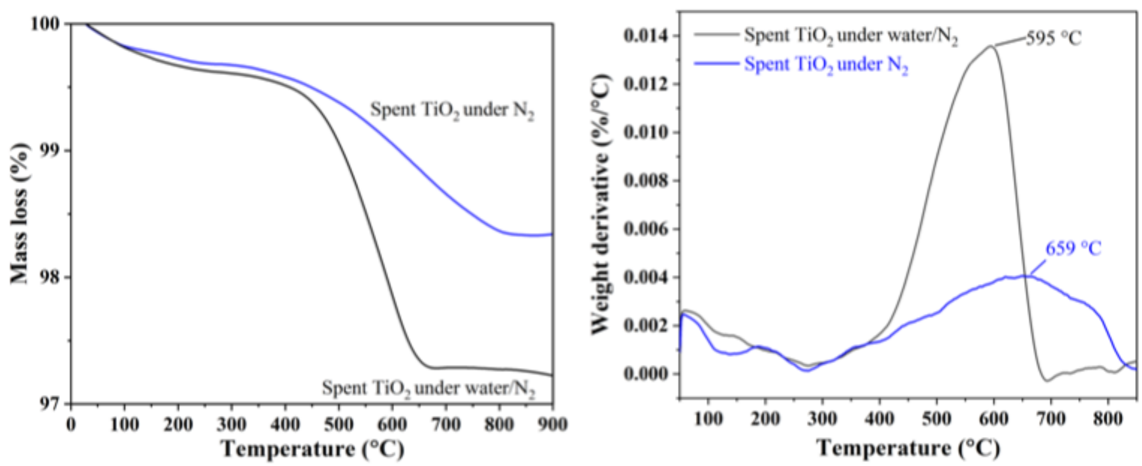

Fig 4.10 TGA of spent TiO_2 from the reaction with/without water co-fed

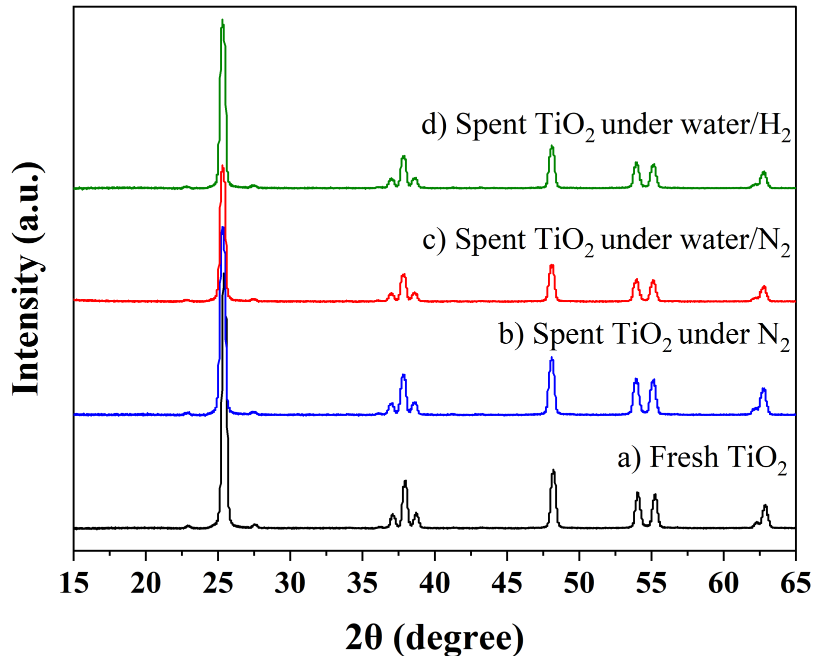

Fig 4.11 XRD of the spent catalysts under various conditions

When H_2 was used as the carrier gas, the product distributions and selectivity remained similar (**Table 4.2, entry 3**). This suggests that the reduction of the catalyst at 400 ℃ before the reaction has completely generated oxygen vacancy/ Ti^{3+} sites on the surface. In other words, no further TiO_2 reduction takes place during the reaction. Hence, no additional Lewis acid site was generated during the ketonization, leading to similar activity. Moreover, the observed unchanged selectivity under H_2 indicated that the ketonization is a non-redox process; otherwise, H_2 would enhance the hydrodeoxygenation of methyl palmitate to C15-C16 hydrocarbons and low oxygenated products. In fact, the selectivity of hydrocarbons in both carrier gases is in a similar range (6.5% in N_2 vs 6.6% in H_2). Nevertheless, the reaction under H_2 with water co-fed (**Fig. 4.8c**) shows a lower deactivation rate compared to that under N_2 (**Fig. 4.8b**). This is presumably due to "softer" coke formation in the reaction under H_2. That is, under H_2 gas the coke formed is more amorphous than under N_2, as evidenced by a lower ID/IG band in Raman spectra of the spent catalysts (**Fig 4.12** and **Table 4.3**).

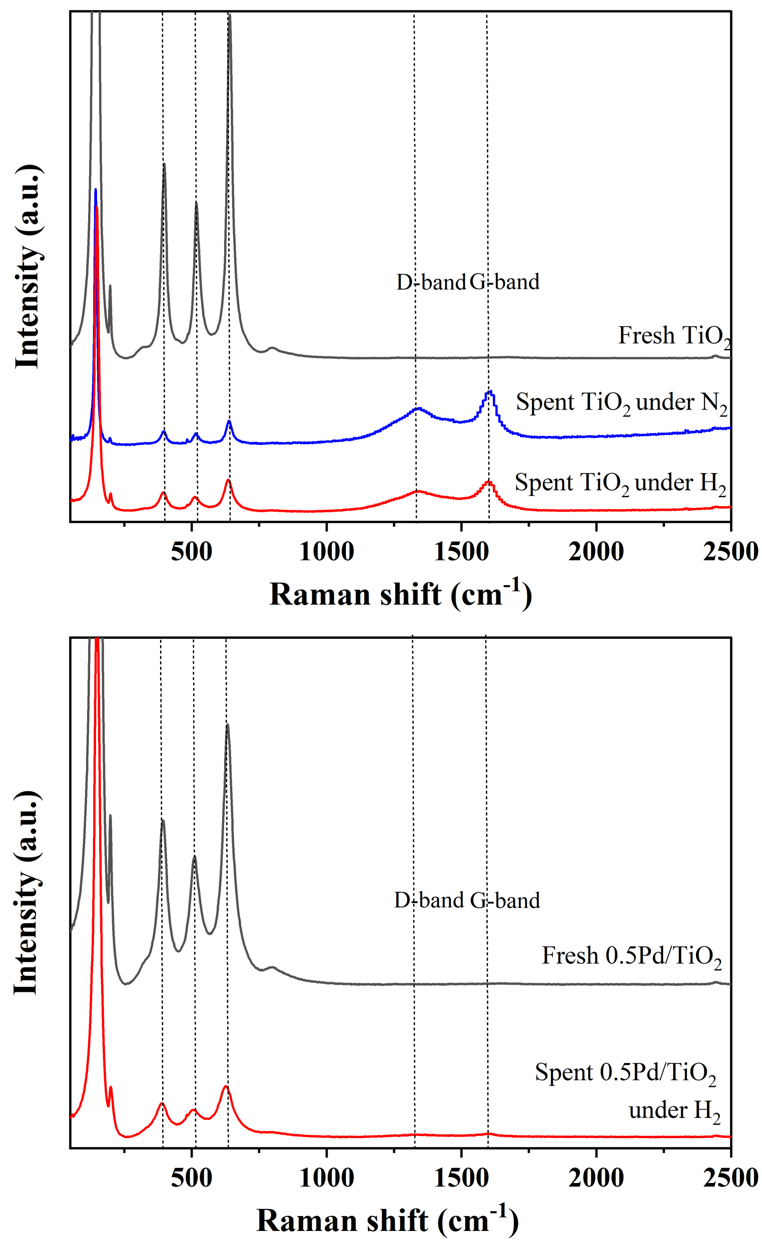

Fig 4.12 Raman spectra of the fresh and spent TiO_2 (a) and 0.5Pd/TiO_2 (b)

Table 4.3 Peak area and D/G band ratio from Raman spectra of the spent TiO_2 under H_2 and N_2 as carrier gas

Entry	Catalyst	Intensity		ID/IG
		D-band	G-band	
1	**Spent TiO_2 under N_2**	708	968	0.73
2	**Spent TiO_2 under H_2**	387	546	0.70

The presence of H_2 as carrier gas may well suppress a successive dehydrogenation of the adsorbed species, preventing the formation of graphitic carbon on the catalyst surface. Moreover, the H_2 can replenish the oxygen vacancy, recovering the active Lewis acid site from a reversed water-gas shift on the surface. Although ketonization is a non-redox process, some of the CO_2 produced from the decomposition of β-keto acid intermediate [20,24] can strongly adsorb on the Ti^{3+} active site (**Scheme 3a**). Despite water co-feeding, the observed deactivation under N_2 gas could result from the redox of the adsorbed CO_2 leaving oxygen on the vacancy, i.e., the reversed water-gas shift [19,27,91]. In support of this view, an increase in CO yield was observed in the reaction under N_2 (**Table 4.2, entry 2)**. While some oxygen vacancies could be regenerated by a reduction in the presence of H_2 as carrier gas (**Scheme 3b**). The water produced from this process can further react with CO via water gas shift reaction to CO_2 and H_2, as seen from a lower CO yield from the reaction under H_2 (**Table 4.2, entry 3**).

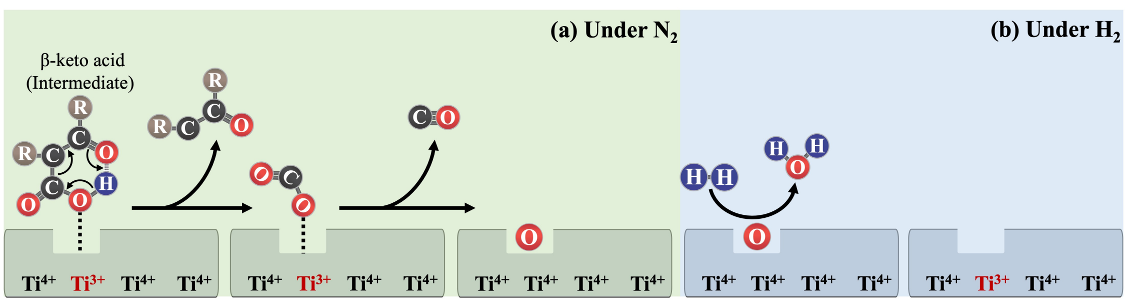

Scheme 3 (a) Redox of CO_2 with oxygen vacancies under N_2 and (b) replenishment of oxygen vacancy site under H_2

4.2.2 Metals loaded TiO_2 catalysts

When TiO_2 sol-gel, a catalyst with a higher surface area (174 m^2/g) was used at the same contact time, the activity and palmitone yield were increased as compared to the anatase TiO_2 (60 m^2/g, **Table 4.4**). However, the selectivity of cracking products was higher, especially for C17 and C29 ketones, despite water co-feeding. This is because TiO_2 sol-gel possessed a relatively higher number of strong acid sites (2.00 μmol/g TiO_2 sol-gel *vs* 0.58

μmol/g TiO_2, **Table 4.1**) that promoted palmitone cracking via McLafferty rearrangement [27,89]. Moreover, a faster deactivation rate was observed over TiO_2 sol-gel (**Fig. 4.13**), presumably due to feed adsorption on the additional strong acid site. This can be deduced from a linear decrease in the mole of methyl palmitate converted/mole of TiO_2 with an increase in the mole of methyl palmitate fed/mole of TiO_2 (**Fig. 4.9**).

Table 4.4 Product distributions after ketonization of methyl palmitate at 400 °C, at 2 hours on stream, W/F = 58 g.h/mol.

Catalyst	Conversion (%)	%Yield (%Selectivity)						
		Palmitone	Palmitic acid	C15-C16 H/C	C13-C14 H/C	C17 and C29 ketone	CO	CO_2
TiO_2	30	13.0 (43.0)	16.0 (53.0)	0.3 (1.0)	0.7 (2.3)	0.3 (1.0)	0.5 (1.7)	3.0 (10)
TiO_2 sol-gel	93	76.0 (82.0)	0.9 (1.0)	2.2 (2.4)	1.7 (1.8)	7.0 (7.5)	2.7 (2.9)	9.6 (10.3)

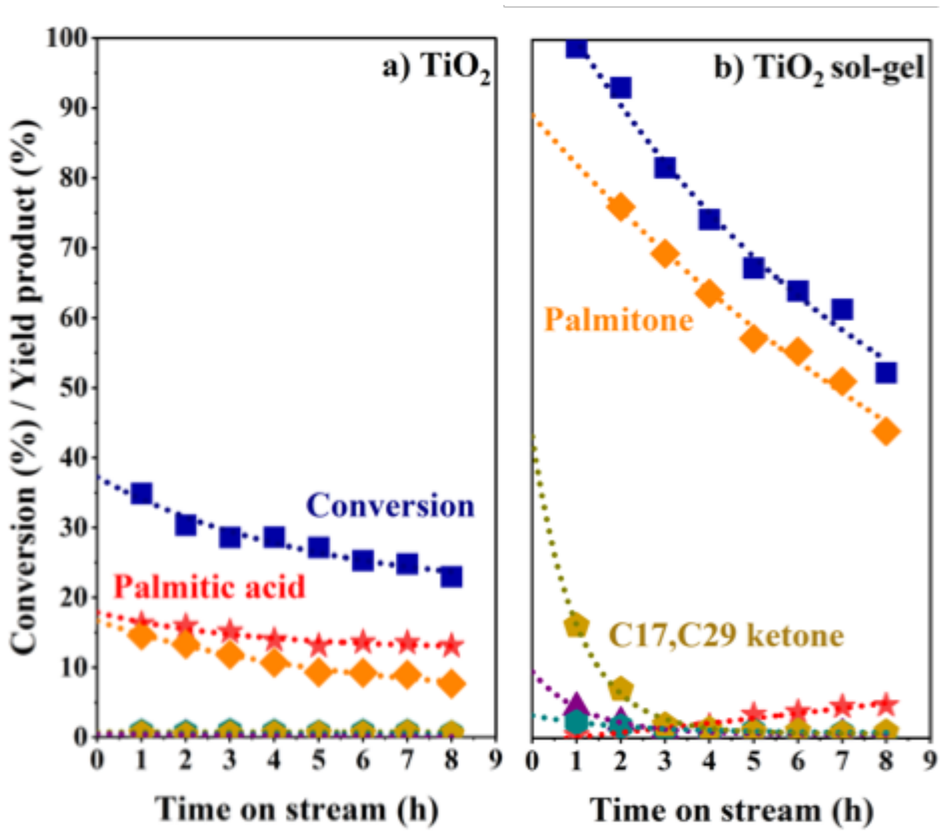

Fig 4.13 *Time on stream profiles for ketonization of methyl palmitate over TiO_2 and TiO_2 sol-gel*

Reaction condition 20%Methyl palmitate in dodecane : 3.1 ml/h, N_2 or H_2 flow rate : 50 ml/min, contact time : 58 gh/mol, activation temperature : 400 °C in air, reduction temperature : 400 °C under H_2, reaction temperature : 400 °C, water : feed ratio 0.24

To minimize the catalyst deactivation, the anatase TiO_2 with a limited number of strong acid sites was incorporated with metals to improve hydrogen dissociation and H_2 spillover on the TiO_2 surface generating higher Ti^{3+} sites. As seen from **Table 4.5,** the conversion of methyl palmitate over 0.5Pt/TiO_2 was significantly improved. However, C15-C16 hydrocarbons (69%) were obtained as major products while small amounts of palmitone (6%) were obtained from the ketonization. This suggested that the rate of hydrodeoxygenation to hydrocarbons and CO [92,93]. is readily promoted over the metallic Pt surface, and faster than that of ketonization over the Ti^{3+} sites. However, the produced CO strongly binds to the Pt surface inhibiting η^1 - C=O adsorption of methyl palmitate. This so-called "CO poisoning" [94,95] suppresses the hydrodeoxygenation resulting in a declined activity with time (**Fig. 4.14b)**. As Pt was deactivated, the methyl palmitate can be activated only by the Lewis acid site as seen by an increased yield of palmitone. Nevertheless, the oxygen vacancy cannot be recovered since the H_2 dissociation and H_2 spillover were hindered by CO poisoning [96]. Accordingly, the palmitone yield from ketonization over 0.5Pt/TiO_2 was lower than that from the parent TiO_2.

Table 4.5 Product distributions after ketonization of methyl palmitate over metal-loaded TiO_2 at 400 °C, at 2 hours on stream, W/F = 232 g.h/mol.

Catalyst	Conversion (%)	%Yield (%Selectivity)						
		Palmitone	Palmitic acid	C15-C16 H/C	C13-C14 H/C	C17 and C29 ketone	CO	CO_2
TiO2	59	46.0 (78.0)	3.0 (5.0)	1.5 (2.5)	1.6 (2.7)	1.0 (1.7)	0.5 (0.8)	3.0 (5.1)
0.5Pt/TiO_2	82	6.0 (7.2)	0.0 (0.0)	69.2 (84.4)	1.7 (2.1)	0.0 (0.0)	6.5 (8.0)	3.7 (4.5)
0.5Ru/TiO_2	67	53.0 (79.1)	0.6 (0.9)	4.8 (7.1)	1.5 (2.2)	1.2 (1.8)	5.4 (8.0)	4.1 (6.1)
0.5Pd/TiO_2	90	77.0 (85.6)	0.0 (0.0)	5.9 (6.6)	1.9 (2.1)	3.2 (3.6)	0.7 (0.8)	5.2 (5.8)

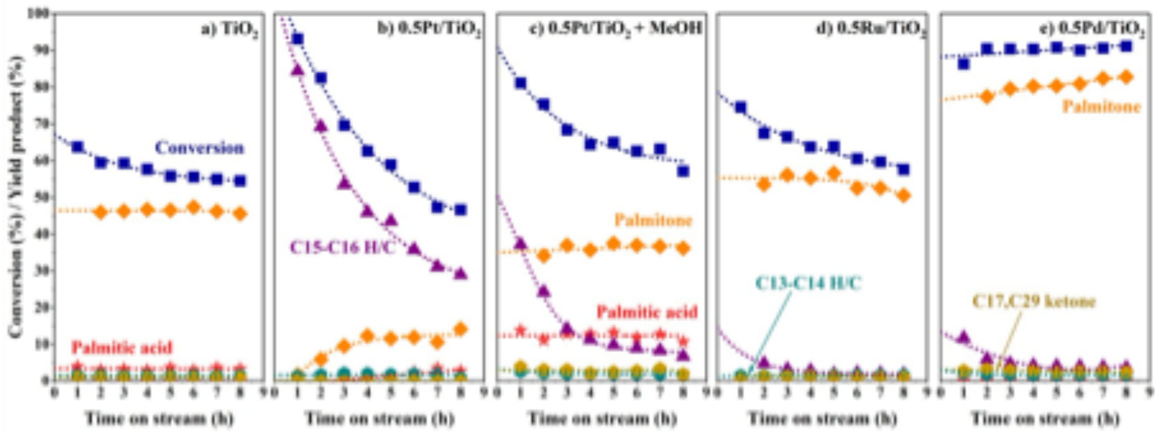

Fig 4.14. Time on stream profiles for ketonization of methyl palmitate over metals incorporated TiO_2 catalysts

Reaction condition 10%Methyl palmitate in dodecane : 3.1 ml/h, N_2 or H_2 flow rate : 50 ml/min, contact time : 232 gh/mol, activation temperature : 400 °C in air, reduction temperature : 400 °C under H_2, reaction temperature : 400 °C, water : feed ratio 0.24 , Methyl palmitate : MeOH 1:1 by mol

To mitigate the hydrodeoxygenation and CO poisoning, a separated reaction with methanol co-fed was tested over $0.5Pt/TiO_2$. It can be seen in **Fig. 4.14c** that C15-C16 hydrocarbons, previously observed over $0.5Pt/TiO_2$, were decreased. In line with this view, relatively less CO was produced (from 6.6 to 2.8% at ~60% conversion) when methanol was co-fed. This suggests that the adsorption and hydrodeoxygenation of methyl palmitate over the metallic Pt surface were suppressed by competitive adsorption of the methanol. Hence, surface CO-Pt species would be reduced, resulting in less CO poisoning and higher stability. The ketonization of methyl palmitate would be predominantly promoted over the Lewis Ti^{3+}, similar to the reaction over bare TiO_2 (**Fig. 4.14a**). However, some of the methyl palmitate may well interact with the Pt surface and undergo hydrogenolysis to palmitic acid as undesired products.

The methyl palmitate conversion over 0.5Ru/TiO_2 (67%) was lower than that of 0.5Pt/TiO_2 (82%). However, palmitone was obtained as a major product (53%) with a lower C15-C16 hydrocarbons yield (4.8%) as shown in **Fig. 4.14d**. A high selectivity of palmitone indicates that the rate of ketonization over the Ti^{3+} sites is higher than the hydrodeoxygenation over the metallic Ru site. The metallic site was responsible only for H_2 dissociation and H_2 spillover [96] to generate the Ti^{3+} site (oxygen vacancy). Accordingly, a higher acidity was observed for 0.5Ru/TiO_2 (12.2 μmol/g), as compared to the parent TiO_2 (10.5 μmol/g) and 0.5Pt/TiO_2 (8.9 μmol/g, **Table 4.1**).

With the same analogy, the higher conversion (90%) and palmitone yield (77%) were obtained over 0.5Pd/TiO_2 (**Fig. 4.14e**). This derives from the superior H_2 dissociation/spillover activity of metallic Pd that results in a higher Ti^{3+} fraction (0.10, **Table 4.1**) and acidity (14.8 μmol/g), as discussed earlier. In particular, the weak and medium acid sites appear to be responsible for the observed high selectivity of palmitone 85.6% over 0.5Pd/TiO_2 catalyst. In support with this view, the linear relationship between the sum of the weak-medium acid site and the sum of the ketonization product was observed in **Fig. 4.15**. This emphasizes the role of surface Lewis Ti^{3+} site on the ketonization activity of these TiO_2-based catalysts [24,97]. In addition, the presence of basic sites also facilitates ketonization, as evidenced by a higher basicity of 0.5Pd/TiO_2, as compared to the TiO_2 support (**Fig. 4.16**).

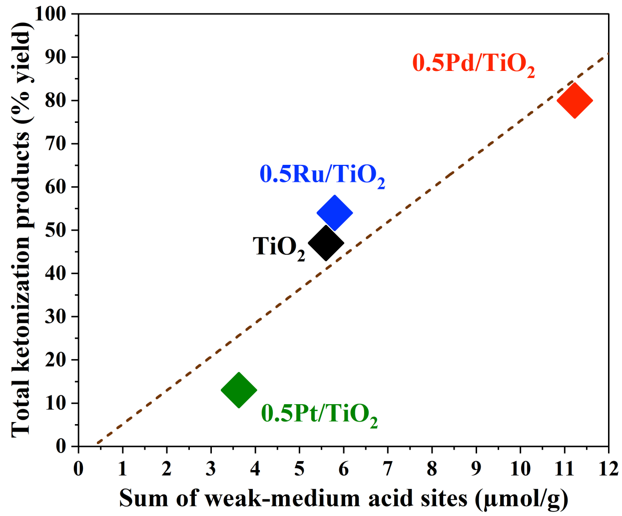

Fig 4.15 The relationship between total ketonization products and the sum of weak-medium acid sites over TiO_2-based catalyst.

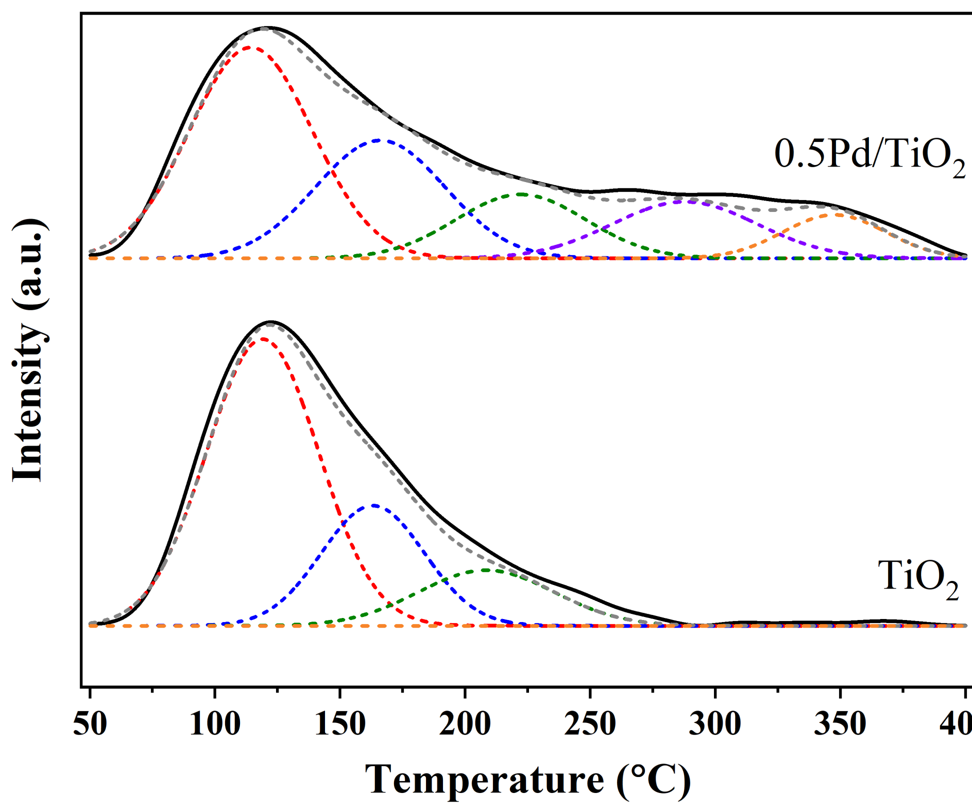

Fig 4.16 *CO_2-TPD profiles and basicity of reduced 0.5Pd/TiO_2 and TiO_2 catalysts*

As the Lewis acid-base density governs the ketonization, the conversion of methyl palmitate and palmitone yield over 0.5Pd/TiO_2 would increase with a contact time **(Fig. 4.17)**. Although the hydrolysis to palmitic acid is initially required for the ketonization (***section 3.2.1***) [20], no palmitic acid was observed at low contact time; palmitone was still produced as a major product. This suggested that the produced palmitic acid strongly adsorbs on the surface and rapidly undergoes ketonization over 0.5Pd/TiO_2. In contrast, the palmitic acid was always observed for the catalyst with lower activity i.e. TiO_2 (**Fig. 4.18**). However, the palmitone yield decreased simultaneously while C17 and C29 ketone yields increased at higher contact time. This is because the palmitone produced can re-adsorb on available Lewis Ti^{3+} sites and undergo cracking to smaller ketone, via McLafferty rearrangement [98]

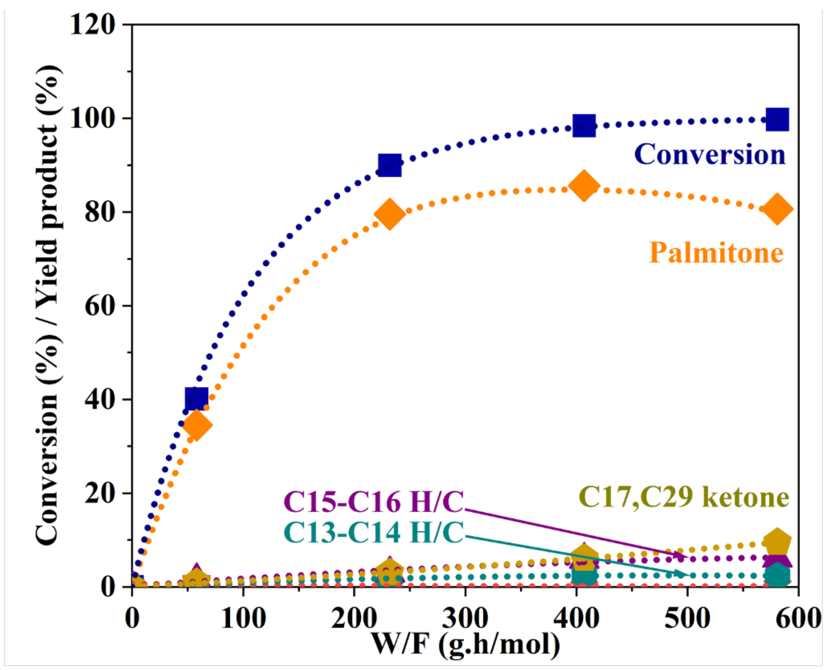

Fig 4.17 Contact time profile on ketonization of methyl palmitate over 0.5Pd/TiO_2

Reaction condition 10%Methyl palmitate in dodecane: 3.1 mL/h, N_2 or H_2 flow rate : 50 mL/min, contact time : 58-581 g.h/mol, activation temperature : 400 °C in air, reduction temperature : 400 °C under H_2, reaction temperature : 400 °C, water : feed ratio 0.24

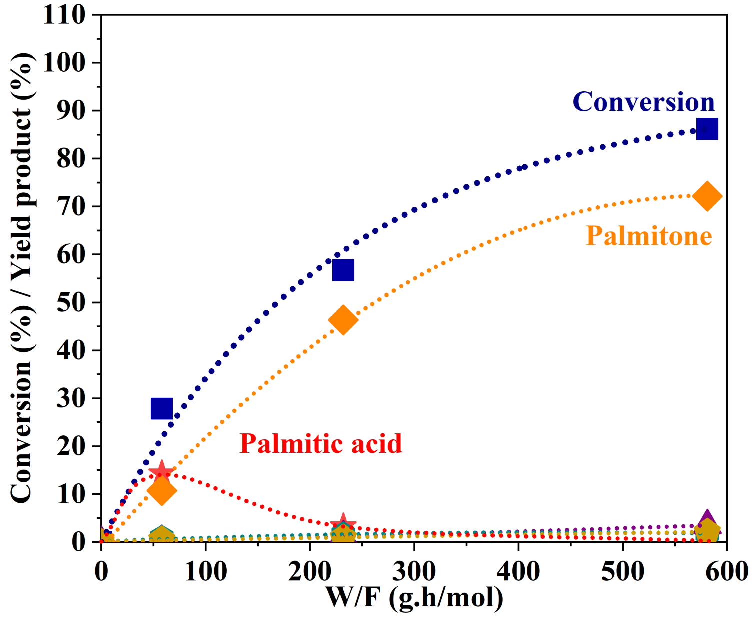

Fig 4.18 Contact time profile on ketonization of methyl palmitate over 0.5Pd/TiO_2

Reaction condition 10%Methyl palmitate in dodecane: 3.1 mL/h, N_2 or H_2 flow rate : 50 mL/min, contact time : 58-581 g.h/mol, activation temperature : 400 °C in air, reduction temperature : 400 °C under H_2, reaction temperature : 400 °C, water : feed ratio 0.24

In addition to ketonization, small amounts of C15 and C16 hydrocarbons were observed in parallel as seen from traces of these products even at low contact time. C15 hydrocarbons could be produced from decarboxylation or decarbonylation of methyl palmitate over the metallic Pd[63,66,99]. As H_2 was present as a carrier gas, hydrodeoxygenation of methyl palmitate [63,99,100] could also be promoted over the metal site to produce C16 hydrocarbons. Accordingly, these products were gradually increased with contact time **(Fig. 4.17)**. The C15-C16 hydrocarbons could further crack over available acid sites to produce lighter products i.e., C13-C14 hydrocarbons as depicted in **Scheme 2.**

Moreover, 0.5Pd/TiO2 showed higher stability compared to other catalysts (**Fig. 4.14e**). This is due to the lower decarbonylation activity of 0.5Pd/TiO2 as seen from lower CO product (0.7% as compared to 5.4% and 6.5% over 0.5Ru/TiO2 and 0.5Pt/TiO2, Table 4). Hence, a lower CO poisoning over metallic Pd could be expected allowing H2 dissociation/spillover over Pd to recover Lewis Ti3+ sites [96]. On the other hand, the hydrodeoxygenation of methyl palmitate to C15-C16 hydrocarbons was readily promoted over 0.5Pt/TiO_2 and 0.5Ru/TiO_2, suppressing recovery of Lewis Ti^{3+} sites as discussed earlier [101]. In addition, Raman spectra of the spent 0.5Pd/TiO_2 show only trace signals of graphitic carbon (D and G bands), as compared to the spent TiO_2 (**Fig 4.12**). This indicates that a negligible amount of coke deposit was formed over 0.5Pd/TiO_2. Accordingly, the methyl palmitate conversion was maintained for up to 26 hours on stream over 0.5Pd/TiO_2 as shown in **Fig. 4.19**. Nevertheless, the lighter ketone yield (C17 and C19 ketone) slightly increased at a longer time on stream. This might be derived from a competitive adsorption of the strongly bound palmitone leading to lighter ketones over the Lewis Ti^{3+} site. From the present study, 0.5Pd/TiO_2 appears to be an active catalyst to produce palmitone, a bio-wax, from methyl palmitate as compared to others reported in the literature (**Table 4.6**).

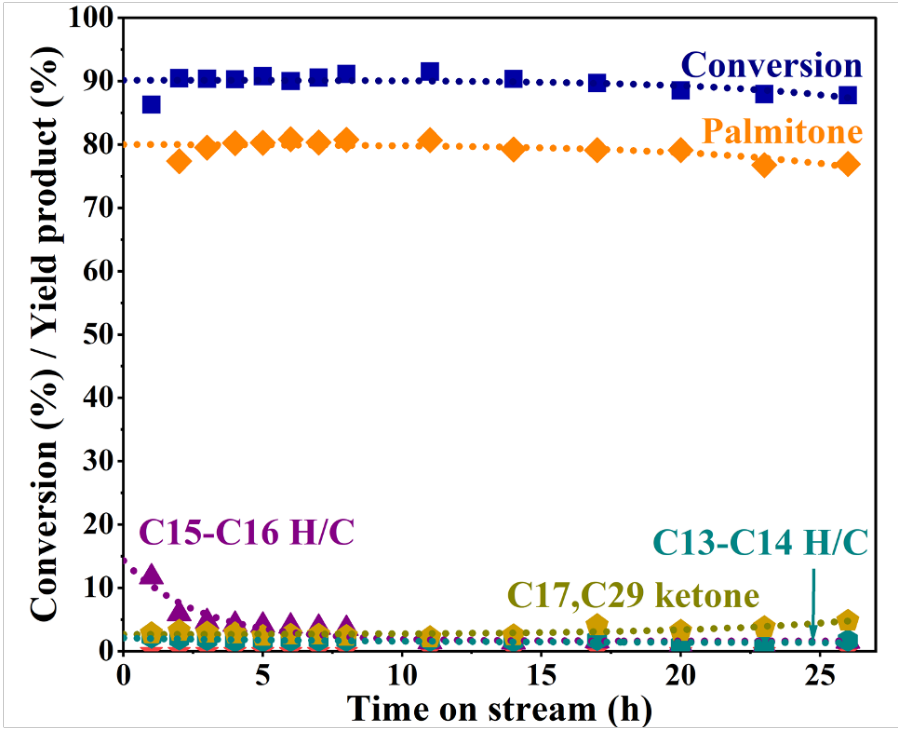

Fig 4.19 Time on stream profile for ketonization of methyl palmitate over $0.5Pd/TiO_2$

Table 4.6 Long-chain ketone selectivity from ketonization over metal oxide-based catalysts.

	Catalyst	Feed	Reactor	Reaction temperature (°C)	Reaction time (h)	WHSV (h^{-1})	Conversion (%)	Ketone selectivity (%)	Ref.
1	$0.5Pd/TiO_2$	10% Methyl palmitate in dodecane	Fixed-bed flow	400	-	1.16	90	85.6	This work
2	TiO_2	10% Methyl palmitate in dodecane	Fixed-bed flow	400	-	1.16	59	78.0	This work
3	TiO_2	10% Methyl palmitate in dodecane	Fixed-bed flow	400	-	2.57	24	50.0	[14]
4	P25 TiO_2	Stearic acid	Plug-flow	380	-	0.50	100	89.0	[66]
5	CeO_2	5% Palmitic acid in p-xylene	Fixed-bed flow	400	-	0.32	100	24.5	[26]
6	M-ZrO_2	Methyl stearate	Fixed-bed flow	400	-	3.02	94	31.9	[67]
7	MnO_2/ZrO_2	Palmitic acid	Semi-batch	340	3	-	92	30.1	[16]
8	La/ZrO_2	Laric acid and Palmitic acid	Batch	380	6	-	80	28.0	[29]

From the reaction throughout the thesis, there was a large amount of waste, so we tried to recrystallize it to separate palmitone from the solvent, including the feed methyl palmitate and other products. The result was palmitone with a purity of up to 97%. When checked by gas chromatography, the remaining 3% was methyl palmitate and palmitic acid. When DSC was performed, it was seen that the melting point was 82 °C, which was the same as the palmitone standard. There was also a sharp peak, indicating that there were no other foreign substances mixed with the recrystallized palmitone shown in **Fig 4.20**.

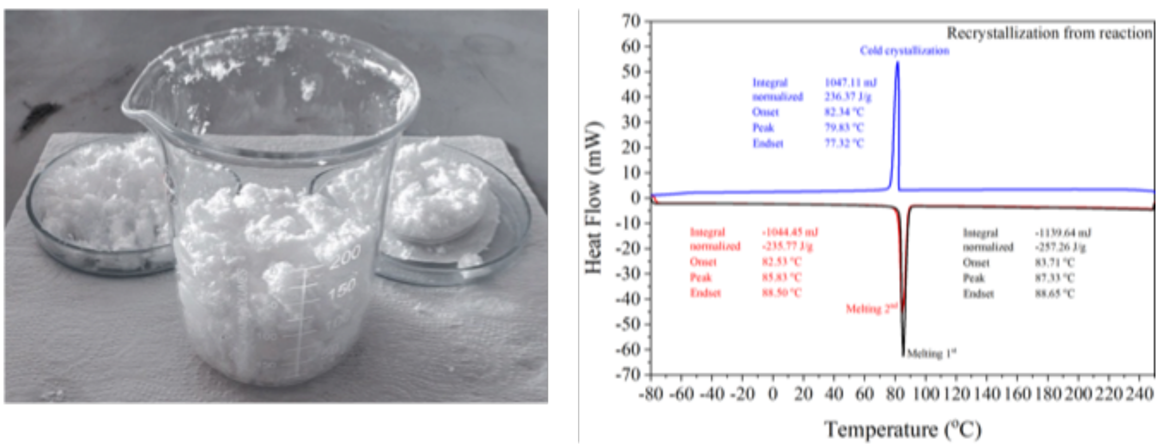

Fig 4.20 Recrystallization of Palmitone from reaction and Differential scanning calorimetry (DSC) of palmitone

Chapter 5

Conclusions and suggestions

5.1 Conclusions

Palmitone, a bio-wax, can be successfully produced from the ketonization of methyl palmitate under H_2 with water co-feeding. Up to 25 hours on stream, 0.5Pd/TiO_2 steadily provides >85% palmitone selectivity with >90% conversion. Water vapor present in the feed stream (~ 0.2 atm) successively promotes the hydrolysis of methyl palmitate to palmitic acid that readily undergoes ketonization to palmitone. In addition, the water suppresses hydrodeoxygenation of methyl palmitate and cracking of the palmitone (McLafferty rearrangement) to lighter products. When using N_2 as a carrier gas, the deactivation was observed from the redox reaction of CO_2 with oxygen vacancy, which led to a continuing decrease in the Lewis Ti^{3+} sites.

The TiO_2 sol-gel with a high surface area shows higher activity under H_2 carrier gas with water co-fed as compared to commercial TiO_2. However, the higher number of strong acid sites enhances the feed adsorption resulting in rapid deactivation. This is also the case in the reaction without water co-feeding. The metals incorporated TiO_2 (Pd, Ru, and Pt) can significantly improve the ketonization activity due to a higher Ti^{3+}. For 0.5Pt/TiO_2, the methyl palmitate preferably adsorbs on the metallic Pt leading to the formation of C15 and lighter hydrocarbons via hydrodeoxygenation and cracking. The CO produced from decarbonylation also causes a faster deactivation of 0.5Pt/TiO_2 due to CO poisoning on the metal sites. Ru and Pd facilitate the H_2 dissociation/spillover on the TiO_2 support, generating more Lewis Ti^{3+} sites, on which the methyl palmitate preferably adsorbs and undergoes ketonization. In particular, the effective H_2 dissociation/spillover activity of Pd offers a continual recovery of Lewis Ti^{3+} sites leading a higher stability as compared to other metals loaded TiO_2.

5.2 Suggestions

5.2.1 In order to verify the effect of water on the reaction, the amount of water would be investigated.

5.2.2 The mechanism will be fulfilled with the computational study.

References

[1] M. Barea-Sepúlveda, J.L.P. Calle, M. Ferreiro-González, M. Palma, Spectrochim. Acta. A. Mol. Biomol. Spectrosc. 310 (2024) 123910.

[2] A.A. Olajire, Chem. Eng. J. Adv. 6 (2021) 100104.

[3] S.K. Kurre, J. Yadav, Ind. Crops Prod. 193 (2023) 116122.

[4] C.-W. Su, L.-D. Pang, M. Qin, O.-R. Lobont, M. Umar, Energy 274 (2023) 127304.

[5] A. Talebian-Kiakalaieh, N.A.S. Amin, H. Mazaheri, Appl. Energy 104 (2013) 683–710.

[6] Y. Wang, Q. Zhang, J. Hao, Z. Luo, J. Xiao, Sustain. Prod. Consum. 37 (2023) 284–293.

[7] E.C.G. Aguieiras, A. Papadaki, A. Mallouchos, I. Mandala, H. Sousa, D.M.G. Freire, A.A. Koutinas, Ind. Crops Prod. 139 (2019) 111499.

[8] J.A. Ribeiro Neto, S.N. Alves, L.A.R.D.S. Lima, Biocatal. Agric. Biotechnol. 50 (2023) 102689.

[9] W. Zhong, F. Yan, J. Wang, W. Gao, G. Xu, Z. He, L. Hua, Q. Wang, Fuel 343 (2023) 127887.

[10] C. Sowcharoensuk, Industry Outlook 2022-2024: Palm oil Industry, 2022.

[11] K. Pindit, A. Thanapimmetha, M. Saisriyoot, P. Srinopakun, Ind. Crops Prod. 166 (2021) 113484.

[12] B.L.A. Prabhavathi Devi, T. Vijai Kumar Reddy, M.F. Mohd Yusoff, in: Ion. Liq. Lipid Process. Anal., Elsevier, 2016, pp. 373–401.

[13] P. Srisanong, P. Daorattanachai, N. Laosiripojana, (2021).

[14] G. Durango-Giraldo, C. Zapata-Hernandez, J.F. Santa, R. Buitrago-Sierra, J. Ind. Eng. Chem. 107 (2022) 31–44.

[15] B. Oliver-Tomas, M. Renz, A. Corma, Ind. Eng. Chem. Res. 56 (2017) 12870–12877.

[16] G. Olarte, L. Garzón, J. Sarmiento, L.J. López-Giraldo, J.C. Vivas-Báez, Processes 11 (2023) 1372.

[17] K. Lee, M.Y. Kim, M. Choi, 38.

[18] R. Kumar, N. Enjamuri, S. Shah, A.S. Al-Fatesh, J.J. Bravo-Suárez, B. Chowdhury, Catal. Today 302 (2018) 16–49.

[19] C.A. Gaertner, J.C. Serrano-Ruiz, D.J. Braden, J.A. Dumesic, J. Catal. 266 (2009) 71–78.

[20] T.N. Pham, T. Sooknoi, S.P. Crossley, D.E. Resasco, ACS Catal. 3 (2013) 2456–2473.

[21] C.A. Gaertner, J.C. Serrano-Ruiz, D.J. Braden, J.A. Dumesic, Ind. Eng. Chem. Res. 49 (2010) 6027–6033.

[22] T. Maluangnont, P. Arsa, K. Limsakul, S. Juntarachairot, S. Sangsan, K. Gotoh, T. Sooknoi, J. Solid State Chem. 238 (2016) 175–181.

[23] A. Guntida, T. Rattanachartnarong, B. Jongsomjit, T. Sooknoi, P. Weerachawanasak, S. Praserthdam, P. Praserthdam, Appl. Catal. Gen. 628 (2021) 118405.

[24] S.A. Aleem, N. Asikin-Mijan, A.S. Hussain, C.H. Voon, A. Dolfi, S. Sivasangar, Y.H. Taufiq-Yap, RSC Adv. 11 (2021) 31972–31982.

[25] B. Boekaerts, (2021).

[26] O. Nagashima, S. Sato, R. Takahashi, T. Sodesawa, J. Mol. Catal. Chem. 227 (2005) 231–239.

[27] T. Maluangnont, C. Dararat, T. Kulrat, S. Soontontaweesub, T. Anothaiwalaikul, P. Bunprechawong, R. Chanda, J. Kanchanawarin, P. Kidkhunthod, T. Sooknoi, Catal. Commun. 102 (2017) 123–126.

[28] Y. Guo, Y. Qin, H. Liu, H. Wang, J. Han, X. Zhu, Q. Ge, ACS Catal. 12 (2022) 2998–3012.

[29] G. Pacchioni, ACS Catal. 4 (2014) 2874–2888.

[30] S. Zaidi, N. Asikin-Mijan, A.S. Hussain, M.S. Mastuli, F.A. Alharthi, A.A. Alghamdi, Y.H. Taufiq-Yap, J. Taiwan Inst. Chem. Eng. 121 (2021) 217–228.

[31] K. Wu, M. Yang, W. Pu, Y. Wu, Y. Shi, H. Hu, ACS Sustain. Chem. Eng. 5 (2017) 3509–3516.

[32] S. Tosoni, G. Pacchioni, J. Catal. 344 (2016) 465–473.

[33] B. Boekaerts, W. Lorenz, J. Van Aelst, B.F. Sels, Appl. Catal. B Environ. 305 (2022) 121052.

[34] M. Elahifard, M.R. Sadrian, A. Mirzanejad, R. Behjatmanesh-Ardakani, S. Ahmadvand, Catalysts 10 (2020) 397.

[35] X. Pan, M.-Q. Yang, X. Fu, N. Zhang, Y.-J. Xu, Nanoscale 5 (2013) 3601.

[36] Z. Shi, L. Lin, R. Chen, L. Yan, Mater. Today Commun. 28 (2021) 102699.

[37] Y. Lu, H. Deng, T. Pan, L. Wang, C. Zhang, H. He, Appl. Surf. Sci. 606 (2022) 154834.

[38] T.N. Pham, D. Shi, T. Sooknoi, D.E. Resasco, J. Catal. 295 (2012) 169–178.

[39] T.N. Pham, D. Shi, D.E. Resasco, J. Catal. 314 (2014) 149–158.

[40] N. Aranda-Pérez, M.P. Ruiz, J. Echave, J. Faria, Appl. Catal. Gen. 531 (2017) 106–118.

[41] V.G. Deshmane, S.L. Owen, R.Y. Abrokwah, D. Kuila, J. Mol. Catal. Chem. 408 (2015) 202–213.

[42] R. Prins, Chem. Rev. 112 (2012) 2714–2738.

[43] J. Hu, E.M. Kim, M.J. Janik, K. Alexopoulos, J. Phys. Chem. C 126 (2022) 7482–7491.

[44] H. Kim, J.H. Park, J.-M. Ha, D.H. Kim, ACS Catal. 13 (2023) 11857–11870.

[45] Y. Zhu, D. Liu, M. Meng, Chem Commun 50 (2014) 6049–6051.

[46] N.H. Mohamed, F.S. Soliman, H. El Maghraby, Y.M. Moustfa, Renew. Sustain. Energy Rev. 70 (2017) 1052–1058.

[47] T. Wu, C. Wang, Y. Hu, X. Zeng, M. Song, Int. J. Heat Mass Transf. 211 (2023) 124202.

[48] Q. Liu, T. Xiao, L. Geng, C. Liu, J. Energy Storage 67 (2023) 107633.

[49] M. Galli, M. Baini, C. Panti, P. Tepsich, M. Rosso, F. Giannini, F. Galgani, M.C. Fossi, J. Hazard. Mater. 467 (2024) 133677.

[50] S. Yousef, J. Eimontas, K. Zakarauskas, N. Striugas, J. Clean. Prod. 290 (2021) 125878.

[51] B. Lesar, P. Kralj, M. Humar, Int. Biodeterior. Biodegrad. 63 (2009) 306–310.

[52] Y. Wang, V. Herdegen, X. Li, J.-U. Repke, Sep. Purif. Technol. 204 (2018) 90–97.

[53] M. González-Bermúdez, Á.I. López-Lorente, R. Lucena, S. Cárdenas, Talanta 273 (2024) 125860.

[54] Z. Han, K. Cheng, Y. Pan, F. Chen, J.-H. Shao, S. Liu, Q. Sun, S. Wei, H. Ji, Food Chem. 458 (2024) 140188.

[55] B. Medjahed, S. Dardouri, O.E. Goual, A. Yüksel, M. Arıcı, S. Chaib, J. Energy Storage 101 (2024) 113898.

[56] K.Z. Hafila, R. Jumaidin, R.A. Ilyas, M.Z. Selamat, F.A.M. Yusof, Int. J. Biol. Macromol. 194 (2022) 851–860.

[57] S. Nurul Syahida, M.R. Ismail-Fitry, Z.M.A. Ainun, Z.A. Nur Hanani, Food Packag. Shelf Life 23 (2020) 100437.

[58] Y. Lan, in: Encycl. Food Chem., Elsevier, 2019, pp. 312–316.

[59] E.R. Gunawan, M. Basri, Mohd.B.Abd. Rahman, A.B. Salleh, R.N.Z.Abd. Rahman, Enzyme Microb. Technol. 37 (2005) 739–744.

[60] K. Demski, B.-J. Ding, H.-L. Wang, T.N.T. Tran, T.P. Durrett, I. Lager, C. Löfstedt, P. Hofvander, Metab. Eng. 72 (2022) 391–402.

[61] Z. Yuan, Y. Wang, G. Zhao, J. Yin, S. Ma, J. Chem. Thermodyn. 188 (2024) 107163.

[62] S.P. Verevkin, A.A. Pimerzin, A.P. Glotov, A.V. Vutolkina, Fuel 329 (2022) 125460.

[63] H. Zuo, Q. Liu, T. Wang, L. Ma, Q. Zhang, Q. Zhang, Energy Fuels 26 (2012) 3747–3755.

[64] A. Gumilar, Therm. Crack. Chem. Eng. Process. (2009).

[65] V.R. Wiggers, R.F. Beims, L. Ender, E.L. Simionatto, H.F. Meier, in: E. Jacob-Lopes, L.Q. Zepka (Eds.), Front. Bioenergy Biofuels, InTech, 2017.

[66] L. Ai, Y. Shi, Y. Han, J. Chen, React. Kinet. Mech. Catal. 133 (2021) 209–227.

[67] X. Cao, F. Long, F. Wang, J. Zhao, J. Xu, J. Jiang, Renew. Energy 180 (2021) 1–13.

[68] W.N.A. Wan Khalit, N. Asikin-Mijan, T.S. Marliza, M. Safa-Gamal, M.R. Shamsuddin, I.N. Azreena, M.I. Saiman, Y.H. Taufiq-Yap, J. Anal. Appl. Pyrolysis 164 (2022) 105505.

[69] Y. Wang, Y. Yu, Y. Yu, F. Huang, J.B. Baell, Adv. Synth. Catal. 365 (2023) 2601–2606.

[70] J. Ji, S. Ai, W. Yu, L. Liu, Y. Qin, Sep. Purif. Technol. 308 (2023) 122979.

[71] Riedel, R. 2004. Handbook of ceramic hand materials. Wiley-VCH: German.

[72] Z. Wang, L. Wang, EcoMat 3 (2021).

[73] Promchana P, 2016 “Mechanistic study on the conversion of fatty acid to long chain olefins over TiO2-based catalysts.” KMITL. 2016. SC. M. 015-015.

[74] W. Tolek, N. Nanthasanti, B. Pongthawornsakun, P. Praserthdam, J. Panpranot, Sci. Rep. 11 (2021) 9786.

[75] L. Fan, Q. Sun, W. Zheng, Q. Tang, T. Zhang, M. Tian, Nanoscale Res. Lett. 15 (2020) 109.

[76] S. Cao, X. Fei, Y. Wen, Z. Sun, H. Wang, Z. Wu, Appl. Catal. Gen. 550 (2018) 20–27.

[77] K. Murakami, Y. Sekine, Phys. Chem. Chem. Phys. 22 (2020) 22852–22863.

[78] D.A. Panayotov, J.T. Yates, Chem. Phys. Lett. 436 (2007) 204–208.

[79] F. Boccuzzi, G. Ghiotti, E. Guglielminotti, (1988) 5.

[80] M. Primet, P. Pichat, M.V. Mathieu, J. Phys. Chem. 75 (1971) 1216–1220.

[81] J. Cai, Y. Zhu, D. Liu, M. Meng, Z. Hu, Z. Jiang, ACS Catal. 5 (2015) 1708–1716.

[82] R.S. Dubey, K.V. Krishnamurthy, S. Singh, Results Phys. 14 (2019) 102390.

[83] K. Thamaphat, P. Limsuwan, B. Ngotawornchai, 42 (2008) 357-361.

[84] M.G. Kim, J.M. Kang, J.E. Lee, K.S. Kim, K.H. Kim, M. Cho, S.G. Lee, ACS Omega 6 (2021) 10668–10678.

[85] B. Bharti, S. Kumar, H.-N. Lee, R. Kumar, Sci. Rep. 6 (2016) 32355.

[86] K. Li, Z. Huang, X. Zeng, B. Huang, S. Gao, J. Lu, ACS Appl. Mater. Interfaces 9 (2017) 11577–11586.

[87] B. Choudhury, M. Dey, A. Choudhury, Int. Nano Lett. 3 (2013) 25.

[88] J. Dhanalakshmi, S. Iyyapushpam, S.T. Nishanthi, M. Malligavathy, D. Pathinettam Padiyan, Adv. Nat. Sci. Nanosci. Nanotechnol. 8 (2017) 015015.

[89] P. Promchana, A. Boonchun, J. T-Thienprasert, T. Sooknoi, T. Maluangnont, Catal. Today 375 (2021) 418–428.

[90] R. Yang, X. Du, X. Zhang, H. Xin, K. Zhou, D. Li, C. Hu, ACS Omega 4 (2019) 10580–10592.

[91] A. Gumidyala, T. Sooknoi, S. Crossley, J. Catal. 340 (2016) 76–84.

[92] M. Snåre, I. Kubičková, P. Mäki-Arvela, K. Eränen, D.Yu. Murzin, Ind. Eng. Chem. Res. 45 (2006) 5708–5715.

[93] J. Zhang, M. Zhang, Z. Jin, J. Wang, Z. Zhang, Appl. Surf. Sci. 258 (2012) 3991–3999.

[94] K. Czupryn, I. Kocemba, J. Rynkowski, React. Kinet. Mech. Catal. 124 (2018) 187–201.

[95] J. Liu, F.R. Lucci, M. Yang, S. Lee, M.D. Marcinkowski, A.J. Therrien, C.T. Williams, E.C.H. Sykes, M. Flytzani-Stephanopoulos, J. Am. Chem. Soc. 138 (2016) 6396–6399.

[96] K. Shun, K. Mori, S. Masuda, N. Hashimoto, Y. Hinuma, H. Kobayashi, H. Yamashita, Chem. Sci. 13 (2022) 8137–8147.

[97] S. Yang, B. Qian, Y. Wang, K. Taira, Q. Zhou, K. Wilson, A.F. Lee, L. Zhang, Appl. Catal. B Environ. 322 (2023) 122106.

[98] T. Maluangnont, P. Praserthdam, T. Sooknoi, RSC Adv. 12 (2022) 34293–34302.

[99] I.V. Deliy, E.N. Vlasova, A.L. Nuzhdin, E.Yu. Gerasimov, G.A. Bukhtiyarova, RSC Adv. 4 (2014) 2242–2250.

[100] A. Ishihara, Y. Tsuchimori, T. Hashimoto, RSC Adv. 11 (2021) 19864–19873.

[101] S. Xu, S. Chansai, S. Xu, C.E. Stere, Y. Jiao, S. Yang, C. Hardacre, X. Fan, ACS Catal. 10 (2020) 12828–12840.

Appendices

Appendix A

B1. Contact time, W/F

$$W/F = \frac{\text{Weight of catalyst (g)}}{\text{Molar feed rate (mol/h)}}$$

In the reaction using 0.5 g TiO_2, feed: 10% W/V methyl palmitate in dodecane (density of *n*-dodecane = 0.75 g/mL, Mw = 270.45 g/mol), with a rate of 3.1 mL/h.

The W/F is calculated as follows:

$$W/F = \frac{\text{0.5 g cat. X 270.45 g/mol feed}}{\text{0.75 g/mL feed X 3.1 mL/h feed X 10\% feed}}$$

$$= \text{581 gh/mol}$$

In a similar manner, the W/F of catalysts with a different catalyst weight and different %W/V feed is calculated.

B2. Material balance – a quantitative description of all materials in the reaction.

$$\text{Material balance} = \frac{\text{Total yield of product}}{\text{Conversion}} \text{ X 100}$$

B3. Conversion - the feed changed after the reaction.

$$\text{\% Conversion} = \frac{\text{Corrected area of initial feed - Corrected of feed at any time}}{\text{Corrected area of initial feed}} \text{X100}$$

B4. Yield - the products that are obtained after the reaction

$$\%\ \text{Yield} = \frac{\text{n x Corrected area of each product}}{\text{Corrected area of initial feed}} \text{X100}$$

n = equivalent mole based on methyl palmitate

B5. Selectivity - the ratio of the desired product formed to the undesired product formed.

$$\%\text{Selectivity} = \frac{\%\text{Yield of each product}}{\%\text{Conversion}} \text{ X 100}$$

Corrected area is a mathematical term where the area of interest is divided by the area of the standard.

$$\text{Corrected area of A} = \frac{\text{Area of A}}{\text{Internal standard}}$$

B6. Response factor (RF) - the ratio between the concentration of a compound being analyzed and the response of the detector to that compound.

$$\text{Response factor of A} = \frac{\dfrac{\text{Weight of A}}{\text{Mw of A}}}{\text{Corrected area of A}}$$

Appendix B

A1. TPR SIGNAL EVALUATION

The electronic signal from the TCD detector during TPR analysis is converted to mmol H_2, employing CuO as a standard. Here, CuO is used because it is a highly-reducible metal with clean and well-known reduction giving Cu metal as a final product following the equation:

$$CuO(s) + H_2(g) \longrightarrow Cu(s) + H_2O(g)$$

An example of the TPR profile of CuO is shown in **Fig A1**.

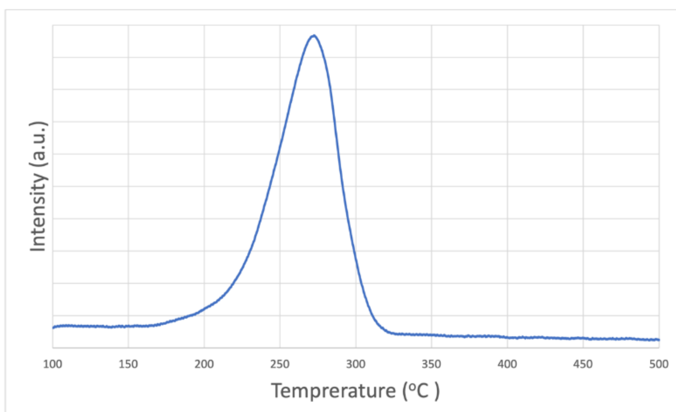

Fig A1 TPR profile of CuO

A few runs were performed by variation of the mass of CuO. Then, the peak area (integrated with Origin Pro 8.0) in the range T = 100-500 °C is plotted against the mole of CuO. The resulting plot (**Fig A2**) serves as a calibration curve where the mmol H_2 of any sample could be calculated from the peak area as shown below.

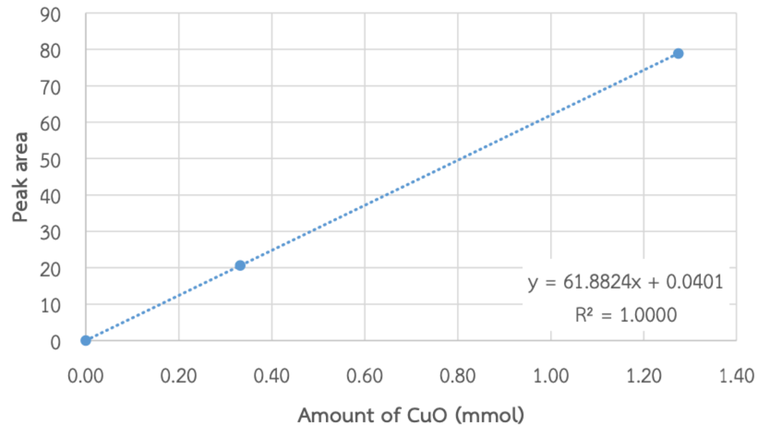

Fig A2 Standard curve of CuO: peak area vs the number of CuO

For example, the peak area of anatase TiO_2 (0.375 g) is 6.4259. Substituting this number into the equation in Figure A2 and solving for x gives:

$$y = 61{,}882.3584x + 0.0401$$

$$6.4259 = 61{,}882.3584x + 0.0401$$

$$x = \text{mmol CuO} = 0.01032 \text{ mmol}$$

As the mole ratio of CuO to H_2 is 1:1, the number of mmol of H_2 consumed by anatase TiO_2 equals 0.01032 mmol as well. So, the reducibility of anatase TiO_2 is 0.01032 mmol H_2/ 0.375 g = 0.02752 mmol H_2/g of catalyst.

Appendix C

C1. Analysis condition

Prior to analysis, the products were classified by GC-MS (Gas chromatography equipped with Mass Spectrometer detector). The analytical conditions of GC-MS from the ketonization of methyl palmitate are shown in **Table C1**. An example of a chromatogram is shown in **Fig C1**. Product identifications are shown in **Table C2**.

Table C1 GC-MS conditions for product analysis from ketonization of methyl palmitate.

Column	HP-5, 30 m x 250 µm x 0.25 µm
Temperature program	40 °C for 3 min to 200 °C at rate 10 °C for 2 min to 280 °C at rate 10 °C for 10 min
Carrier gas	Helium gas
Injector	250 °C
Injection volume	0.1 µL
Detector	FID (290 °C)

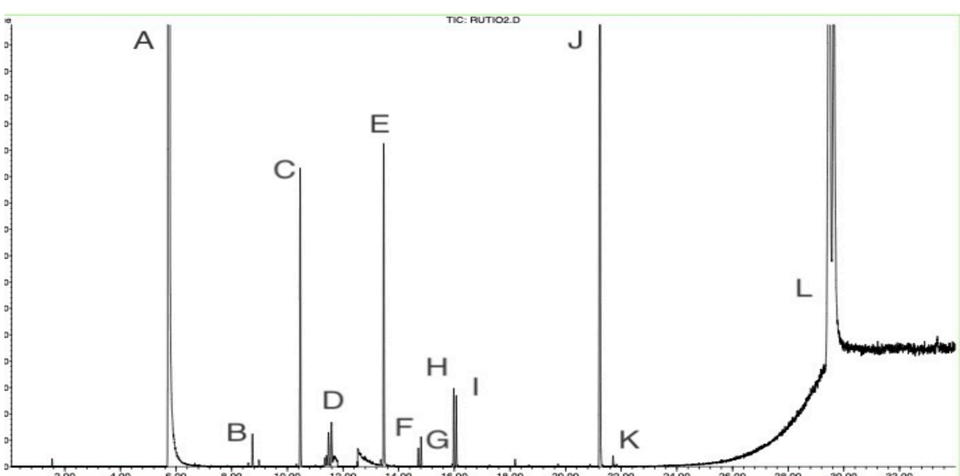

Fig C1 The chromatogram from the ketonization of methyl palmitate

(Reaction condition; reduced TiO_2, feed: 10% W/V methyl palmitate in dodecane, Temperature 400 °C, a flow rate of H_2 carrier gas: 50 mL/min, contact time: 512 g.h/mol), result at 1 h of time on stream)

C2 List of contact time

Table C2 Products distribution from the ketonization of methyl palmitate, according to GC-MS analysis shown in **Fig C1**.

Order	Retention time (min)	Chemical name
A	5.7	Chlorobenzene
B	8.7	n-Decane
C	11.5	C11 alkane
D	13.2	3-Methyl undecane
E	13.4	C13 alkane
F	14.7	Trans- C14 alkane
G	14.8	C14 alkane
H	15.9	C15 alkene
I	16.0	C15 alkane
J	21.2	Methyl palmitate
K	21.6	Palmitic acid
L	29.4	Palmitone

Then, quantitative analysis was carried out with GC-FID (Gas chromatography equipped with Flame ionization Detector). The analytical conditions of products from the ketonization of methyl palmitate are shown in **Table C3**, and this is summarized in **Table C5**. An example of a chromatogram is shown in **Fig C2**.

Table C3 GC conditions for liquid product analysis from ketonization of methyl palmitate.

Column	HP-5MS, 30 m x 320 μm x 0.25 μm
Temperature program	60 °C for 1 min to 210 °C at rate 5 °C to 280 rate 10 °C for 10 min
Carrier gas	Nitrogen gas
Injector	300 °C
Injection volume	0.1 μL
Detector	FID (300 °C)

Then, quantitative analysis was carried out with GC-TCD (Gas chromatography equipped with a Thermal conductivity Detector). The analytical conditions of products from the ketonization of methyl palmitate are shown in **Table C4**, and this is summarized in **Table C6**. An example of a chromatogram is shown in **Fig C3**.

Table C4 GC conditions for gas product analysis from ketonization of methyl palmitate.

Column	PoraPLOT Q-HT, 27.5m x 0.32 mm x 10 µm
Temperature program	30 °C for 5 min to 170 °C at rate 10 °C to 250 rate 5 °C
Carrier gas	Helium
Injector	250 °C
Injection volume	100 µL
Detector	TCD (200 °C)

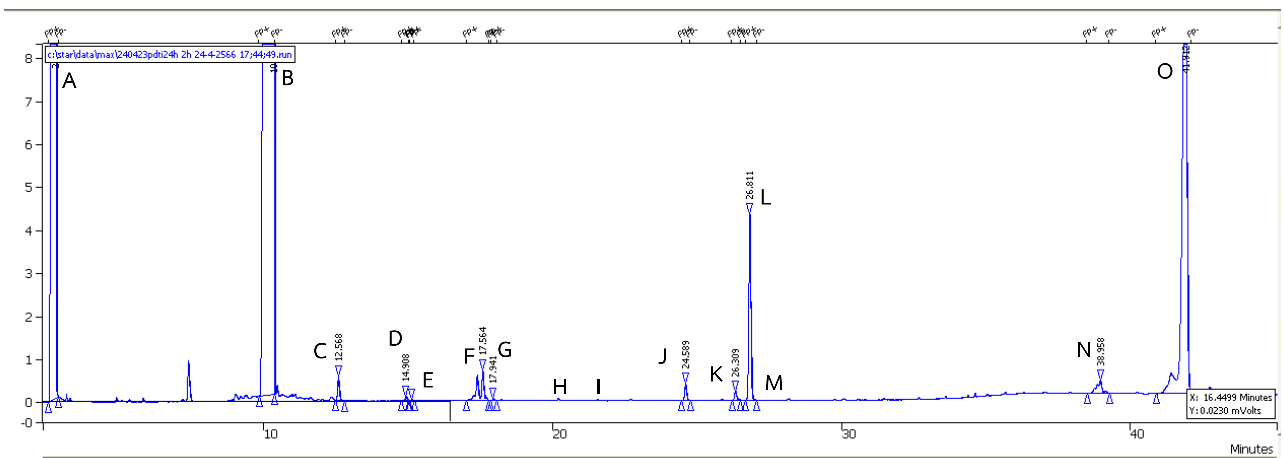

Fig C2 The chromatogram from the ketonization of methyl palmitate

(Reaction condition; reduced $0.5Pd/TiO_2$, feed: 10% W/V methyl palmitate in dodecane, Temperature 400 °C, a flow rate of H_2 carrier gas: 50 mL/min, contact time: 232 g.h/mol), result at 2 h of time on stream)

Table C5 Liquid products distribution from the ketonization of methyl palmitate.

Order	Retention time (min)	Chemical name
A	3.0	Chlorobenzene
B	10.8	Dodecane
C	13.1	C13 alkane
D	15.4	C14 alkene
E	15.6	C14 alkane
F	17.8	C15 alkene
G	18.0	C15 alkane
H	20.2	C16 alkene
I	22.0	C16 alkane
J	24.6	C14 aldehyde
K	26.3	C17 ketone
L	26.8	Methyl palmitate
M	27.4	Palmitic acid
N	39.0	C29 ketone
O	42.0	Palmitone

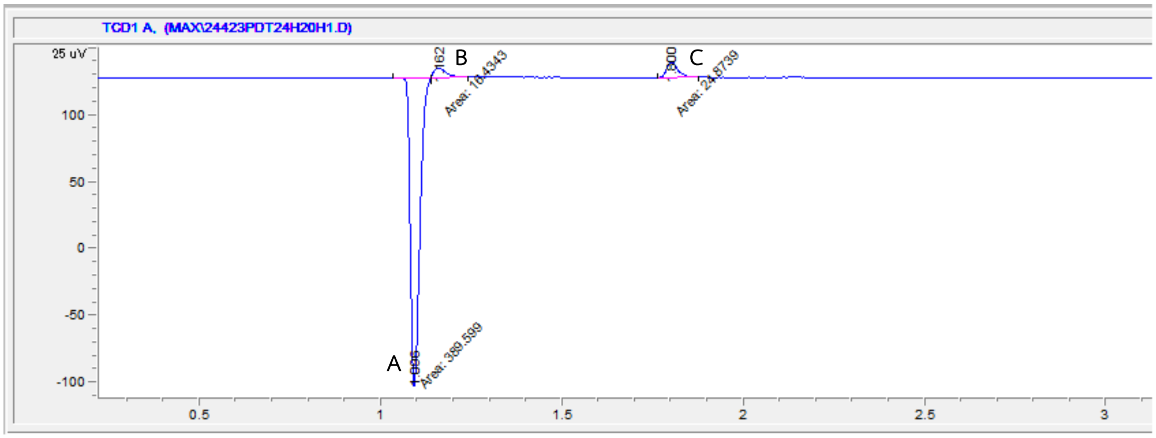

Fig C3 The chromatogram from the ketonization of methyl palmitate

(Reaction condition; reduced 0.5Pd/TiO_2, feed: 10% W/V methyl palmitate in dodecane, Temperature 400 °C, a flow rate of H_2 carrier gas: 50 mL/min, contact time: 232 g.h/mol), result at 2 h of time on stream)

Table C6 Gas product distribution from the ketonization of methyl palmitate.

Order	Retention time (min)	Chemical name
A	1	Hydrogen
B	1.1	Carbon monoxide
C	1.2	Methane
D	1.7	Carbon dioxide

Appendix D

Table D1 NH_3-TPD of reduced catalysts

Entry	Catalyst	Acidity (μmol/g)		
		Weak	Medium	Strong
1	TiO_2	3.70	1.90	0.58
2	$0.5Pt/TiO_2$	2.83	0.80	1.50
3	$0.5Ru/TiO_2$	4.20	1.60	0.60
4	$0.5Pd/TiO_2$	6.93	4.30	1.29
5	TiO_2 sol-gel	4.67	2.44	2.00

Table D2 *CO_2-TPD profiles and basicity of reduced 0.5Pd/TiO_2 and TiO_2 catalysts*

Entry	Catalyst	Basicity (µmol/g)			
		Weak (<120 °C)	**Medium** (120-200 °C)	**Strong** (>200 °C)	**Total**
1	**TiO_2**	2.92	1.20	0.47	4.6
2	**0.5Pd/TiO_2**	2.39	1.41	2.05	5.9

Table D3 Time on stream for ketonization of methyl palmitate over TiO_2 without water under N_2 W/F 581 g.h/mol

Time on stream	Conversion (%)	%Yield				
		Palmitone	Palmitic acid	C15-C16 H/C	C13-C14 H/C	C17 and C29 ketone
1	83	31.0	0.2	10.0	3.0	3.1
2	57	23.0	0.3	6.0	2.3	1.4
3	34	20.0	0.1	4.0	2.1	1.2
4	20	11.0	0	3.0	2.0	0.8
5	18	10.0	0	2.3	2.0	0.8
6	16	10.0	0	1.6	1.7	0.6
7	11	6.0	0	1.3	1.7	0.5
8	8	2.0	0	1.1	1.7	0.5

Table D4 Time on stream for ketonization of methyl palmitate over TiO_2 with water under N_2 W/F 581 g.h/mol

Time on stream	Conversion (%)	%Yield				
		Palmitone	Palmitic acid	C15-C16 H/C	C13-C14 H/C	C17 and C29 ketone
1	93	-	0.2	4.4	2.5	3.6
2	90	70.0	0.1	3.6	2.3	2.8
3	83	68.0	0.1	3.1	2.2	2.3
4	80	69.0	0.1	2.8	2.1	2.2
5	75	63.0	0.1	2.6	2.0	1.8
6	72	62.0	0.1	2.3	2.0	1.7
7	71	58.0	1.4	2.3	2.0	2.0
8	67	57.0	0.9	2.1	1.9	1.5

Table D5 Time on stream for ketonization of methyl palmitate over TiO_2 with water under H_2 W/F 581 g.h/mol

Time on stream	Conversion (%)	%Yield				
		Palmitone	Palmitic acid	C15-C16 H/C	C13-C14 H/C	C17 and C29 ketone
1	95	-	0	4.9	2.1	4.0
2	94	74.0	0	4.3	1.9	3.2
3	91	77.0	0	4.0	1.8	2.7
4	89	71.0	0.3	3.6	1.9	2.4
5	85	70.0	0.6	3.4	1.8	2.0
6	83	70.0	1.4	3.1	1.8	1.5
7	81	71.0	1.7	3.0	1.7	1.6
8	78	69.0	2.8	2.7	1.8	1.4

Table D6 Time on stream for ketonization of methyl palmitate over TiO_2 with water under H_2 W/F 58 g.h/mol

Time on stream	Conversion (%)	%Yield				
		Palmitone	Palmitic acid	C15-C16 H/C	C13-C14 H/C	C17 and C29 ketone
1	34	14.6	16.2	0.4	0.8	0.5
2	30	13.0	16.0	0.3	0.7	0.3
3	28	11.8	15.1	0.2	0.9	0.5
4	28	10.7	14.0	0.2	0.8	0.5
5	27	9.3	13.1	0.2	0.7	0.5
6	25	9.2	13.6	0.1	0.8	0.5
7	24	9.0	13.5	0.1	0.8	0.6
8	22	7.6	13.1	0.1	0.6	0.5

Table D7 Time on stream for ketonization of methyl palmitate over TiO_2 sol-gel with water under H_2 W/F 58 g.h/mol

Time on stream	Conversion (%)	%Yield				
		Palmitone	Palmitic acid	C15-C16 H/C	C13-C14 H/C	C17 and C29 ketone
1	99	-	0.4	4.4	2.3	16.1
2	93	76.0	0.9	2.2	1.7	7.0
3	81	69.0	0.9	1.1	1.3	1.9
4	74	63.0	1.7	0.8	1.1	1.3
5	67	57.0	3.3	0.6	1.1	1.0
6	64	55.0	3.7	0.7	0.9	1.0
7	61	51.0	4.5	0.6	0.8	0.7
8	52	44.0	4.7	0.4	0.8	0.9

Table D8 Time on stream for ketonization of methyl palmitate over TiO_2 with water under H_2 W/F 232 g.h/mol

Time on stream	Conversion (%)	%Yield				
		Palmitone	Palmitic acid	C15-C16 H/C	C13-C14 H/C	C17 and C29 ketone
1	63	-	4.0	1.7	1.6	1.0
2	59	46.0	3.0	1.5	1.6	1.0
3	59	46.2	3.2	1.2	1.5	0.9
4	57	46.6	3.0	1.2	1.5	0.9
5	55	46.4	3.6	1.1	1.5	1.0
6	55	47.0	3.0	1.0	1.5	0.9
7	54	46.0	3.6	1.0	1.5	0.9
8	54	45	3.3	0.9	1.5	0.9

Table D9 Time on stream for ketonization of methyl palmitate over 0.5Pt/TiO_2 with water under H_2 W/F 232 g.h/mol

Time on stream	Conversion (%)	%Yield				
		Palmitone	Palmitic acid	C15-C16 H/C	C13-C14 H/C	C17 and C29 ketone
1	93	1.6	0.0	84.3	1.3	0.3
2	82	6.0	0.0	69.2	1.7	0.0
3	69	9.5	0.0	53.4	2.1	0.0
4	62	12.2	0.0	45.8	2.0	0.0
5	58	11.5	0.8	43.4	1.8	0.2
6	52	12.0	2.4	35.7	1.9	0.0
7	47	10.6	3.5	31.0	1.9	0.0
8	46	14.1	2.7	29.0	0.9	0.0

Table D10 Time on stream for ketonization of methyl palmitate over $0.5Pt/TiO_2$ with water under H_2 MeOH W/F 232 g.h/mol

Time on stream	Conversion (%)	%Yield				
		Palmitone	Palmitic acid	C15-C16 H/C	C13-C14 H/C	C17 and C29 ketone
1	81	-	13.7	37.1	2.6	3.8
2	75	34.0	11.1	24.1	2.2	3.0
3	68	37.0	13.0	14.1	2.0	3.0
4	64	35.0	12.7	11.3	2.0	2.1
5	65	37.0	13.2	9.7	2.0	2.4
6	62	37.0	11.8	9.0	1.9	2.7
7	63	36.0	12.7	8.3	1.8	3.3
8	57	36.0	10.6	6.7	1.8	1.8

Table D11 Time on stream for ketonization of methyl palmitate over $0.5Ru/TiO_2$ with water under H_2 W/F 232 g.h/mol

Time on stream	Conversion (%)	%Yield				
		Palmitone	Palmitic acid	C15-C16 H/C	C13-C14 H/C	C17 and C29 ketone
1	74	-	0.1	-	1.5	0.6
2	67	53.0	0.6	4.8	1.5	1.2
3	66	56.0	0.9	3.1	1.7	1.3
4	63	55.0	0.9	2.7	1.6	1.4
5	63	56.0	0.8	1.9	1.6	1.2
6	60	52.0	0.9	2.1	1.6	1.1
7	59	52.0	0.8	2.0	1.6	1.1
8	57	50.0	0.8	1.8	1.6	1.0

Table D12 Time on stream for ketonization of methyl palmitate over 0.5Pd/TiO_2 with water under H_2 W/F 232 g.h/mol

Time on stream	Conversion (%)	%Yield				
		Palmitone	Palmitic acid	C15-C16 H/C	C13-C14 H/C	C17 and C29 ketone
1	86	-	0.0	11.7	2.2	2.8
2	90	77.0	0.0	5.9	1.9	3.2
3	90	79.0	0.0	4.6	1.8	2.9
4	90	80.0	0.0	4.2	1.6	2.8
5	90	80.0	0.0	4.0	1.6	2.4
6	90	80.0	0.0	3.9	1.7	2.6
7	90	82.0	0.0	3.7	1.7	2.6
8	91	82.0	0.0	3.5	1.7	2.4

Table D13 Time on stream for ketonization of methyl palmitate over 0.5Pd/TiO_2 with water under H_2 MeOH W/F 232 g.h/mol Stability

Time on stream	Conversion (%)	%Yield				
		Palmitone	Palmitic acid	C15-C16 H/C	C13-C14 H/C	C17 and C29 ketone
1	86	-	0.0	11.7	2.2	2.8
2	90	77.0	0.0	5.8	1.9	3.2
3	90	79.0	0.0	4.6	1.8	2.9
4	90	80.0	0.0	4.2	1.6	2.8
5	90	80.0	0.0	4.0	1.6	2.4
6	90	80.0	0.0	3.9	1.7	2.6
7	90	80.0	0.0	3.7	1.7	2.6
8	91	80.0	0.0	3.5	1.7	2.4
11	91	80.0	0.0	1.4	1.7	2.2
14	90	79.0	0.0	1.4	1.6	2.5
17	89	79.0	0.0	1.5	1.8	4.1
20	88	79.0	0.0	0.8	1.0	3.2
23	87	79.0	0.0	0.8	0.9	3.8
26	87	76.0	0.0	1.5	1.7	4.8

Table D14 Contact time on ketonization of methyl palmitate over TiO_2 with water under

Contact time (gh/mol)	Conversion (%)	%Yield				
		Palmitone	Palmitic acid	C15-C16 H/C	C13-C14 H/C	C17 and C29 ketone
0	0	0	0	0	0	0
58	27	10.0	14.3	0.2	0.7	0.5
232	56	46.0	3.2	1.1	1.5	0.9
581	86	72.0	1.0	3.5	1.8	2.1

H_2

Table D15 Contact time on ketonization of methyl palmitate over 0.5Pt/TiO_2 with water under H_2

Contact time (gh/mol)	**Conversion (%)**	**%Yield**				
		Palmitone	**Palmitic acid**	**C15-C16 H/C**	**C13-C14 H/C**	**C17 and C29 ketone**
0	0	0	0	0	0	0
232	56	11.0	1.6	39.7	1.7	0.0
581	90	54.0	0.8	30.5	2.7	1.2

Table D16 Contact time on ketonization of methyl palmitate over $0.5Ru/TiO_2$ with water under H_2

Contact time (gh/mol)	Conversion (%)	%Yield				
		Palmitone	Palmitic acid	C15-C16 H/C	C13-C14 H/C	C17 and C29 ketone
0	0	0	0	0	0	0
232	62	52	0.8	2.6	1.5	1.1
407	80	67	3.2	5.3	2.3	2.2
581	93	79	0.1	5.1	1.6	2.9

Table D17 Contact time on ketonization of methyl palmitate over $0.5Pd/TiO_2$ with water under H_2

Contact time (gh/mol)	Conversion (%)	%Yield				
		Palmitone	Palmitic acid	C15-C16 H/C	C13-C14 H/C	C17 and C29 ketone
0	0	0	0	0	0	0
58	40	34.0	1.3	1.4	0.7	0.9
232	89	79.0	0.0	2.9	1.5	3.0
407	98	85.0	0.0	5.8	2.5	6.1
581	99	80.0	0.2	6.1	2.3	9.5

Table D18 Methyl palmitate converted vs fed per mole of TiO_2 in the catalyst bed

TiO_2		TiO_2 sol-gel	
Methyl palmitate fed/ TiO_2 (mol/mol)	Methyl palmitate converted/ TiO_2 (mol/mol)	Methyl palmitate fed/ TiO_2 (mol/mol)	Methyl palmitate converted/ TiO_2 (mol/mol)
0.15	0.13	0.31	0.30
0.31	0.09	0.63	0.29
0.47	0.05	0.94	0.25
0.62	0.03	1.26	0.23

Table D19 The relationship between total ketonization product and the sum of weak-medium acid sites over TiO_2-based catalyst

Catalyst	Sum of weak-medium acid sites (μmol/g)	Total ketonization product (%yield)
TiO_2	5.6	47.0
0.5Pt/TiO_2	3.6	13.0
0.5Ru/TiO_2	5.8	54.0
0.5Pd/TiO_2	11.2	80.0

Author Biography

Name Jetsadagorn Pittayatornkul

Date of Birth 13 August 1998

Address 165/322 Phimon Rat, Bang bua thong, Nonthaburi

Education (2020) Bachelor of Science Program in Industrial Chemical, King Mongkut's Institute of Technology Ladkrabang

Publication Water-assisted ketonization of methyl palmitate to palmitone over metals incorporated TiO_2 catalysts, Jetsadagorn Pittayatornkul, Tosapol Maluangnont, Siriporn Jongpatiwut, Piyasan Praserthdam, Makoto Ogawa and Tawan Sooknoi, Reaction Chemistry & Engineering, 2024